

Ab initio study of electron transport in lead
telluride

by

Qichen Song

Submitted to the Department of Mechanical Engineering
in partial fulfillment of the requirements for the degree of

Master of Science in Mechanical Engineering

at the

MASSACHUSETTS INSTITUTE OF TECHNOLOGY

February 2018

© Massachusetts Institute of Technology 2018. All rights reserved.

Author
Department of Mechanical Engineering
Jan 16, 2018

Certified by
Gang Chen
Carl Richard Soderberg Professor of Power Engineering
Thesis Supervisor

Accepted by
Rohan Abeyaratne
Chairman, Department Committee on Graduate Students

Ab initio study of electron transport in lead telluride

by

Qichen Song

Submitted to the Department of Mechanical Engineering
on Jan 16, 2018, in partial fulfillment of the
requirements for the degree of
Master of Science in Mechanical Engineering

Abstract

Last few years have witnessed significant enhancement of thermoelectric figure of merit of lead telluride (PbTe) via nanostructures. Despite the experimental progress, current understanding of the electron transport in PbTe is based on either band structure simulated using first-principles in combination with constant relaxation time approximation or empirical models, both requiring adjustable parameters obtained by fitting experimental data.

This thesis aims to compute thermoelectric properties of PbTe all from first-principles. We start by discussing the formalism based on Boltzmann transport equation to calculate the electron transport properties in PbTe using first principles and identify the importance to calculate electron-phonon interaction accurately. We then discuss the challenges in studying electron-phonon interaction in semiconductors using first-principles and introduce electron-phonon Wannier interpolation which allows us to calculate the strength of electron-phonon coupling on a very fine mesh. In polar materials like PbTe, the Fröhlich interaction due to long-range dipole field of longitudinal optical phonons contributes to the electron-phonon coupling as well. As the long-range nature of the dipole field makes the standard Wannier interpolation fail, we have discussed the detailed procedures for correction. Next, we study the screening effect of free carriers on electron transport by modulating the polar scattering. These considerations enabled us to report parameter-free first-principles calculation of electron and phonon transport in PbTe, including mode-by-mode electron-phonon scattering, leading to detailed information on electron mean free paths and the cumulative contributions by electrons and phonons with different mean free paths to thermoelectric transport properties in PbTe. Such information will help to rationalize the use and optimization of nanosstructures to achieve high thermoelectric figure of merit.

Thesis Supervisor: Gang Chen

Title: Carl Richard Soderberg Professor of Power Engineering

Acknowledgments

I would like to thank my advisor, Professor Gang Chen for providing the guidance and source for my research. He initiates the direction of this project and allows me to conduct research in my own way. His critical thinking on this research topic not only helps me identify critical issues but inspires me to become a thorough researcher.

I want to thank Professor David Broido at Boston College, Professor Gerald Denise Mahan, Professor Zhifeng Ren at University of Houston, Professor Boris Kozinsky at Harvard, Professor Qian Zhang at Harbin Institute of Technology, Professor Bolin Liao at UCSB, and Professor Mingda Li at MIT for the insightful discussions.

Also, I am thankful for my lab mates, Doctor Te-Huan Liu, Jiawei Zhou, Yoichiro Tsurimaki, Samuel Huberman, Doctor Jonathan Mendoza and Qian Xu for the useful discussions. I want to thank Ms. Keke Xu and Ms. Juliette A. Pickering for the assistance in the laboratory.

I am very thankful for the funding support from DOE S3TEC. The center provides fantastic collaborative working and DARPA MATRIX program for supporting the computational code development.

I am grateful for my friends Haozhe Wang, Dr. Meng An for the encouraging my pursuit of this work. In particular, I would like to express my appreciation for the generous support of my life from my girlfriend, Mengying Wu.

Last but not least, I want to thank my family. When pursuing this degree, I have not been able to come back home for more than two years while my parents show great patience and endless love to me. Such unconditional love means so much to me.

Contents

1	Introduction	15
1.1	Motivations for nanostructuring the thermoelectric materials	16
1.2	Electron transport properties of interest in thermoelectric materials . .	18
1.2.1	Linearized Boltzmann transport equation for electrons	19
1.2.2	Electron transport properties and electron mean free paths	20
1.3	Electron scattering rate	25
1.4	A brief review of previous computational work	28
1.5	Outline of the thesis	30
2	Lattice dynamics from first principles	31
2.1	Density functional theory	31
2.1.1	Hartree approximation	32
2.1.2	Hartree-Fock approximation	33
2.1.3	Kohn-Sham equation, local density approximation and pseudopotentials	34
2.2	Density functional perturbation theory	36
2.2.1	Linear response theory	37
2.2.2	General form of perturbed potential	38
2.3	Phonons in polar materials	38
2.3.1	Nonanalytical force constant in polar materials	39
2.3.2	The screening effect of free carriers on phonons	40
2.3.3	Phonon dispersion of PbTe with different carrier concentrations	42

3 Electron-phonon interaction in from first principles	45
3.1 Electron-phonon interaction to the lowest order	46
3.2 Electron-phonon Wannier interpolation	47
3.2.1 Maximumly localized Wannier function	47
3.2.2 Electron-phonon coupling matrix in the Wannier representation	49
3.3 Electron-phonon coupling matrix in polar materials	50
3.3.1 Screened Fröhlich interaction	50
3.3.2 Electron-phonon coupling matrix for different phonon polarization in PbTe	52
3.4 Relaxation time approximation	55
3.4.1 Electron-phonon scattering rate	55
3.4.2 Phonon scattering rate by electrons	57
4 The electron mean free paths and transport properties in PbTe	61
4.1 <i>Ab initio</i> thermoelectric transport properties	62
4.1.1 The effect of screening	62
4.1.2 The effect of temperature	64
4.2 Weakly isotropic scattering rates in PbTe	69
5 Summary and future work	73
5.1 Summary	73
5.2 Future work	74
5.2.1 Symmetry analysis on the electron-phonon coupling matrix . .	74
5.2.2 Scattering by the grain boundary	75
A Lindhard dielectric function	77
B Anisotropic effective mass of electrons	85
C Phonon thermal conductivity from first principles	89

List of Figures

1-1	The origin of the long-range dipole field due to LO phonon in polar material consisting two atoms per unit cell.	28
2-1	The screening effect of free carriers on the optical phonon modes. At the limit of $q \rightarrow 0$, the LO and TO modes converges given strong enough screening effect	41
2-2	The inverse of the Thomas-Fermi wavevector ($1/k_{TF}$) — screening radius as a function of carrier density from DFT and from parabolic band model.	42
2-3	The phonon dispersion for different free carrier concentrations compared with neutron scattering experiment[10].	44
3-1	The maximumly localized Wannier orbitals of Pb and Te in PbTe without spin-orbit coupling. The symmetry of the material is not conserved during the iterative process of minimizing the localization functional.	49
3-2	The amplitude of the electron-phonon coupling matrix element for electron at conduction band minimum and phonons at the high-symmetry paths with/without considering screening in the long-range (Fröhlich) part of the electron-phonon coupling matrix. The carrier concentration is 10^{18} cm^{-3}	53

3-3	The amplitude of the electron-phonon coupling matrix element including screening effect for electrons at $L \rightarrow \Gamma$ path and LO/TO phonons at $\Gamma \rightarrow L$. In (a) and (c), different colors mark different electron states. In (b) and (d), the strength of the coupling between Γ point LO/TO phonon and different electron states are shown. Note that for LO phonon, the exact $q = 0$ behavior cannot be calculated due to the divergence shown in Eq. 3.14 thus we use $q = 0.01 \times l_{\Gamma L} = 0.01 \times \frac{\sqrt{3}\pi}{2a}$ to represent the extreme case $q = 0$. The carrier concentration is 10^{18} cm^{-3} .	54
3-4	(a-b) The energy-resolved electron-phonon scattering rates for conduction band electrons due to phonon modes of different branches at 300 K with/without considering the screening effect. The zero energy marks the conduction band minimum and the dashed line indicates the location of chemical potential. The carrier concentration is $2.3 \times 10^{19} \text{ cm}^{-3}$.	56
3-5	The scattering rate for phonons due to electron-phonon interaction compared with the scattering rate due to phonon-phonon interaction at 300 K with the carrier concentration of 10^{21} cm^{-3} .	58
4-1	(a) The mobility, (b) the electrical conductivity, (c) the Seebeck coefficient, and (d) the power factor of PbTe as a function of carrier concentration at 300 K with and without considering the screening effect. Dotted lines are from simulation and isolated dots are experimental value. The triangles are from Ref.[26], squares from Ref.[54], diamonds from Ref.[67], and crosses from Ref.[15].	63

4-2 (a) The electron mean free path as a function of energy with and without considering the screening effect. The dashed line indicates the chemical potential and zero energy indicates the conduction band minimum. (b) The accumulated electrical conductivity with respect to electron mean free path. (c) The normalized truncated Seebeck coefficient with respect to the electron mean free path. (d) The normalized truncated power factor with respect to electron mean free path compared with normalized accumulated phonon thermal conductivity with respect to phonon mean free path. The dopant concentration is $2.3 \times 10^{19} \text{ cm}^{-3}$	65
4-3 The electron mean free path as a function of energy at different temperatures. The dashed line indicates the chemical potential and zero energy corresponds the conduction band minimum. The dopant concentration is $5.8 \times 10^{19} \text{ cm}^{-3}$	66
4-4 (a) The accumulated electrical conductivity with respect to electron mean free path. The normalized truncated (b) Seebeck coefficient and (c) power factor with respect to electron mean free path. (d) The accumulated lattice thermal conductivity with respect to phonon mean free path. The dopant concentration is $5.8 \times 10^{19} \text{ cm}^{-3}$	67
4-5 (a) The conductivity, (b) the Seebeck coefficient, (c) the electronic thermal conductivity compared with phonon thermal conductivity, (d) the bipolar thermal conductivity, (e) the total thermal conductivity and (f) the figure of merit zT of PbTe as a function of temperature for different ionized donor concentrations. The squares are experimental results from Ref.[54]	69
4-6 Electron-phonon scattering rates for different phonon polarizations mapped into the electron band structure. L → W is light-mass direction and L → Γ is the heavy mass-direction.	71

List of Tables

B.1	The longitudinal and transverse effective mass of PbTe from calculation and experiment[31]	86
B.2	The DOS and conductivity effective mass of PbTe from calculation and experiment[42]	87

Chapter 1

Introduction

Heat and electricity are two forms of energy both playing essential roles in our life. Electricity is the phenomena regarding the flow of charge. It is controllable, versatile and energizes all kinds of equipment. Heat, on the other side, is the process regarding the flow of thermal energy. It originates from the stochastic motion of atoms measured by temperature thus can be found everywhere. The demand for electricity stimulates several thermal-to-electrical energy conversion technologies, such as thermionics, thermoelectrics, and thermophotovoltaics. The thermionics/thermophotovoltaics involve spontaneous emission of electrons/photons such that they both require a high-temperature heat source. In contrast, thermoelectric devices can work at various temperature ranges. As a result, thermoelectric devices are considered as potential candidates to convert waste heat into useful electricity. To realize such applications, a comprehensive understanding of the physical process happening inside the thermoelectric devices is crucial. In solid-state thermoelectric materials, electricity is carried by either electrons or holes while heat is carried by energy carriers including electrons, holes, phonons, magnons. The essences of thermoelectric effects are transport phenomena of those carriers. The study of the transport process is indeed a study of the interplay of the charge and heat carriers.

A typical thermoelectric device composes of an *n*-doped and a *p*-doped semiconductor “leg” combined between the heat source and sink. The carriers in each leg are driven out of equilibrium by the temperature gradient to form a flow. In *n*-doped

semiconductors, electrons are thermally excited at the hot side and diffuse towards the cooler side. An electrical potential difference is generated correspondingly. Such phenomenon is named as Seebeck effect and the Seebeck coefficient is $S = -\Delta V/\Delta T$. Meanwhile, phonons are migrating from the heat source towards sink. During the nonequilibrium transport process, the electrons/holes are charge and heat carriers, and phonons are heat carriers. From a thermodynamics point of view, to maximize the efficiency of thermoelectric power generator, we want the work — electrical power to be maximized, and less heat dumped into the heat sink. In other words, higher electrical conductivity, larger Seebeck coefficient and lower thermal conductivity at the same time are desired.

1.1 Motivations for nanostructuring the thermoelectric materials

In 1993, L. D. Hicks and M. S. Dresselhaus pointed out in two pioneering papers[28][29] that a quantum-well structure and one-dimensional conductor can significantly increase the figure of merit zT , a dimensionless quantity that measures the thermoelectric performance of the material. Essentially, in low-dimension thermoelectric materials, the density of states near the conduction/valence band edge are much higher than their three-dimensional bulk correspondent[13]. These findings inspired people to think of controlling materials at nanoscale and brought profound changes to the thermoelectric community. From the 1940s to 1990s, the maximum zT was only slowly increasing over time from about 0.1 to about 1. After 1993 when the idea of nanostructuring was proposed, the zT value has been increasing with time, eventually above 2.5[27]. Past works have also successfully increased the thermoelectric efficiency by reducing the phonon thermal conductivity. In silicon, for example, the electron mean free paths from first-principles calculation are around tens of nanometers[58], while phonons have mean free paths up to a few microns[14]. As a result, nanostructures with grain sizes between the electron and phonon mean free path strongly

scatter phonons and reduce thermal conductivity dramatically yet have minimal effects on the electrical transport[58]. Such kind of enhancement of thermoelectric performance has also been observed in the experiment for nanocrystalline silicon[52]. Compared with low-dimensional nanostructures, the bulk nanostructuring approach might be applied in more general conditions[33].

The first-principles calculation scheme much facilitated the understanding of phonon transport and the phonon thermal conductivity in nanostructures. In such scheme, the lattice dynamics is obtained by either supercell approach (real space) or density functional perturbation approach (reciprocal space). By solving the linearized phonon Boltzmann transport equation either iteratively[37] or adopting relaxation time approximation, the behavior of each phonon mode can be resolved. The *ab initio* calculation of intrinsic phonon transport shows excellent agreement with experiment[71]. With the detailed information of phonon such as phonon mean free paths, experimentalists know what the expected grain size is that the phonon are much more efficiently scattered. However, this is only one side of the story. To avoid any deterioration of electron transport due to the nanostructures, the information on electron dynamics is needed. Surprisingly, a fully first-principles calculation for electron transport with a similar level of details for phonons is rarely reported. This motivates us to find an accurate approach to calculate the electron transport properties with mode-by-mode resolution.

Several groups reported high figure of merit in PbTe through different nanostructuring approaches [78][6][55][56][77]. One beneficial feature of PbTe is its low intrinsic thermal conductivity due to the strong anharmonicity[12][35][70]. For PbTe, the thermal transport has also been examined from the first principles yielding that phonons with mean free paths smaller than 10 nm contribute the majority of the thermal conductivity. This implies that to reduce the thermal conductivity, the grain sizes should be in the order of magnitude of 10 nm. Biswas *et al.* proposed a “panoscopic” approach that mesoscale grain boundaries ($10^0 — 10^3$ nm) can scatter phonons with different mean free paths. As a result, they claim that the maximum reduction of the thermal conductivity is achieved. Meanwhile, the electrical transport properties

are not compromised. Particularly, the Seebeck coefficient slightly increases. A phenomenological model by Martin has attribute it to interface barrier scattering[46]: the interface barrier that impedes low-energy electron conduction between grains leads to enhanced Seebeck coefficient. Due to the lack of intrinsic electron mean free path calculation, such model is yet to be justified. To understand the origin of the outstanding performance of nanostructured PbTe, we believe it is necessary to carry out the first-principles calculation of electron transport properties.

1.2 Electron transport properties of interest in thermoelectric materials

The maximum efficiency of a thermoelectric device is defined by,

$$\eta_{\max} = \frac{T_H - T_C}{T_C} \frac{\sqrt{1 + Z\bar{T}} - 1}{\sqrt{1 + Z\bar{T}} + \frac{T_C}{T_H}}, \quad (1.1)$$

where T_H and T_C are the absolute temperatures of hot side and cold side, and \bar{T} is the average temperature defined by $(T_H + T_C)/2$. The larger the temperature difference between the hot side and cold side and the higher the average figure of merit $Z\bar{T}$, the higher the efficiency of the thermoelectric devices is. The figure of merit at temperature T is only related to material properties as,

$$zT = \frac{\sigma S^2 T}{\kappa} \quad (1.2)$$

where σ is the electrical conductivity, S is the Seebeck coefficient, κ is the thermal conductivity consisting the contribution from electrons (κ_e), ambipolar diffusion (κ_{bp}) and phonons (κ_{ph}), and T is the temperature. In the following, the microscopic description of these quantities is shown.

1.2.1 Linearized Boltzmann transport equation for electrons

We start the derivation by writing down the Boltzmann transport equation for electrons,

$$\frac{\partial f_{n\mathbf{k}}}{\partial t} + \mathbf{v}_{n\mathbf{k}} \cdot \nabla_{\mathbf{r}} f_{n\mathbf{k}} + \mathbf{F}_{n\mathbf{k}} \cdot \nabla_{\mathbf{p}} f_{n\mathbf{k}} = \left. \frac{df_{n\mathbf{k}}}{dt} \right|_{\text{coll}}, \quad (1.3)$$

where $f_{n\mathbf{k}}$ is the distribution function of the electron with band index n and momentum \mathbf{k} . The force acted by electric field is $\mathbf{F}_{n\mathbf{k}} = q\mathbf{E}$ where $q = -e$ for electrons and $q = +e$ for holes. To simplify Eq 1.3, we make following approximations:

- The applied electrical field and temperature gradient are weak enough that the distribution function is slightly deviated from equilibrium. Also, the characteristic time scale of the variation of the distribution function is slow, such that the term $\partial f_{n\mathbf{k}}/\partial t \approx 0$.
- The existence of the external electrical field and temperature gradient only lead to small deviation of the distribution function from its equilibrium state. Electron is Fermion obeying Fermi-Dirac distribution at equilibrium as $f_{n\mathbf{k}}^0 = 1/(\exp((\varepsilon_{n\mathbf{k}} - \mu)/k_B T) + 1)$, where μ is the chemical potential. When out of equilibrium, the gradient of the distribution function is determined by the equilibrium distribution via, $\nabla_{\mathbf{r}} f_{n\mathbf{k}} \approx \nabla_{\mathbf{r}} f_{n\mathbf{k}}^0$ and $\nabla_{\mathbf{p}} f_{n\mathbf{k}} \approx \nabla_{\mathbf{p}} f_{n\mathbf{k}}^0 = \nabla_{\mathbf{p}} \varepsilon_{n\mathbf{k}} \frac{\partial f_{n\mathbf{k}}^0}{\partial \varepsilon_{n\mathbf{k}}} = \mathbf{v}_{n\mathbf{k}} \frac{\partial f_{n\mathbf{k}}^0}{\partial \varepsilon_{n\mathbf{k}}}$.
- The form of the collision term $(df_{n\mathbf{k}}/dt)|_{\text{coll}}$ depends on the type of interaction involved. However, we can define a characteristic time $\tau_{n\mathbf{k}}$ to estimate the collision term as $-\frac{f_{n\mathbf{k}}^0 - f_{n\mathbf{k}}}{\tau_{n\mathbf{k}}}$. This is known to be relaxation time approximation.

With these approximations, the Eq. 1.3 writes,

$$\mathbf{v}_{n\mathbf{k}} \cdot \left(\nabla_{\mathbf{r}} f_{n\mathbf{k}}^0 + q\mathbf{E} \frac{\partial f_{n\mathbf{k}}^0}{\partial \varepsilon_{n\mathbf{k}}} \right) = -\frac{f_{n\mathbf{k}}^0 - f_{n\mathbf{k}}}{\tau_{n\mathbf{k}}}. \quad (1.4)$$

Taking the advantage of the form of Fermi-Dirac distribution, we have,

$$\nabla_{\mathbf{r}} f_{n\mathbf{k}}^0 = -\frac{\partial f_{n\mathbf{k}}^0}{\partial \varepsilon_{n\mathbf{k}}} \left(\nabla_{\mathbf{r}} \mu - \nabla_{\mathbf{r}} \varepsilon_{n\mathbf{k}} + \frac{\varepsilon_{n\mathbf{k}} - \mu}{T} \nabla_{\mathbf{r}} T \right). \quad (1.5)$$

Here, we always choose the conduction band minimum E_c as the energy reference for electrons[8]. Assuming the band structure is not changed when the carrier concentration is changed (rigid band approximation), the electron energy is only depending on the band index and wavevector thus $\nabla_{\mathbf{r}}\varepsilon_{n\mathbf{k}} = 0$. The gradient of E_c is also the gradient of electrostatic potential energy. As a result, we realize that $q\mathbf{E} = -q\nabla_{\mathbf{r}}\phi = -\nabla_{\mathbf{r}}E_c$. Note that the chemical potential μ is also defined with respect to the conduction band minimum. The electrochemical potential is the sum of chemical potential and electrostatic potential as, $\Phi = \mu + q\phi = \mu + E_c$. By plugging Eq.1.5 into Eq.1.4, the Boltzmann transport equation becomes,

$$\mathbf{v}_{n\mathbf{k}} \cdot \left[-\nabla_{\mathbf{r}}(\mu + q\phi) - \frac{\varepsilon_{n\mathbf{k}} - \mu}{T} \nabla_{\mathbf{r}}T \right] \frac{\partial f_{n\mathbf{k}}^0}{\partial \varepsilon_{n\mathbf{k}}} = -\frac{f_{n\mathbf{k}}^0 - f_{n\mathbf{k}}}{\tau_{n\mathbf{k}}}. \quad (1.6)$$

Reorganizing this equation, we obtain the nonequilibrium distribution function,

$$f_{n\mathbf{k}} = f_{n\mathbf{k}}^0 - \mathbf{v}_{n\mathbf{k}} \tau_{n\mathbf{k}} \left[-\nabla_{\mathbf{r}}\Phi - \frac{\varepsilon_{n\mathbf{k}} - \mu}{T} \nabla_{\mathbf{r}}T \right]. \quad (1.7)$$

1.2.2 Electron transport properties and electron mean free paths

The electrical current is defined by the charge carried by all electron states per area per unit time,

$$\mathbf{J}_c = \frac{1}{N\Omega} \sum_{n\mathbf{k}} q\mathbf{v}_{n\mathbf{k}} f_{n\mathbf{k}}, \quad (1.8)$$

where N is the total number of the electron states $n\mathbf{k}$ and Ω the volume of the unit cell. The deviation of the distribution function $f_{n\mathbf{k}} - f_{n\mathbf{k}}^0$ is an asymmetric function of wavevector \mathbf{k} and the equilibrium distribution $f_{n\mathbf{k}}^0$ is a symmetric function of \mathbf{k} . As a result, the electrical current is only determined by the deviation of the distribution function,

$$\mathbf{J}_c = -\frac{1}{N\Omega} \sum_{n\mathbf{k}} q\mathbf{v}_{n\mathbf{k}} \left[-\nabla_{\mathbf{r}}\Phi - \frac{\varepsilon_{n\mathbf{k}} - \mu}{T} \nabla_{\mathbf{r}}T \right] \quad (1.9)$$

Similarly, the heat flux — the energy flow carried by electrons per area per unit time writes,

$$\mathbf{J} = -\frac{1}{N\Omega} \sum_{n\mathbf{k}} (\varepsilon_{n\mathbf{k}} - \mu) \mathbf{v}_{n\mathbf{k}} \left[-\nabla_{\mathbf{r}} \Phi - \frac{\varepsilon_{n\mathbf{k}} - \mu}{T} \nabla_{\mathbf{r}} T \right] \quad (1.10)$$

The charge flux and the heat flux are correlated with the temperature gradient and electrochemical potential gradient by the transport coefficients,

$$\mathbf{J}_c = -\mathbf{L}_{11} \cdot \left(\frac{1}{q} \nabla_{\mathbf{r}} \Phi \right) - \mathbf{L}_{12} \cdot \nabla_{\mathbf{r}} T. \quad (1.11)$$

$$\mathbf{J} = -\mathbf{L}_{21} \cdot \left(\frac{1}{q} \nabla_{\mathbf{r}} \Phi \right) - \mathbf{L}_{22} \cdot \nabla_{\mathbf{r}} T. \quad (1.12)$$

The first term in Eq. 1.11 describes the electrical current due to the electrochemical potential gradient and the coefficient \mathbf{L}_{11} is the electrical conductivity tensor. By matching the terms in Eq.1.9 and Eq.1.11, we find that,

$$\sigma_{\alpha\beta} = L_{\alpha\beta}^{11} = -\frac{q^2}{\Omega N} \sum_{n\mathbf{k}} v_{n\mathbf{k}\alpha} v_{n\mathbf{k}\beta} \tau_{n\mathbf{k}} \frac{\partial f_{n\mathbf{k}}^0}{\partial \varepsilon_{n\mathbf{k}}}, \quad (1.13)$$

where α and β are certain directions in Cartesian coordinates. By changing the condition for the summation from $\{n\mathbf{k}\}$ to $\{n\mathbf{k}, |\mathbf{v}_{n\mathbf{k}}| \tau_{n\mathbf{k}} < \lambda\}$, we obtain the contribution to the conductivity of electrons with mean free paths up to a given value λ ,

$$\sigma_{\alpha\beta}(\lambda) = L_{\alpha\beta}^{11} = -\frac{q^2}{\Omega N} \sum_{l_{n\mathbf{k}} \leq \lambda} v_{n\mathbf{k}\alpha} v_{n\mathbf{k}\beta} \tau_{n\mathbf{k}} \frac{\partial f_{n\mathbf{k}}^0}{\partial \varepsilon_{n\mathbf{k}}}, \quad (1.14)$$

where the mean free path of electron $n\mathbf{k}$ is $l_{n\mathbf{k}} = |\mathbf{v}_{n\mathbf{k}} \tau_{n\mathbf{k}}|$. Note that we can break the summation into the summation over electron states and hole states separately, and obtain electron conductivity $\sigma_{\alpha\beta}^e$ and hole conductivity $\sigma_{\alpha\beta}^h$ by,

$$\sigma_{\alpha\beta}^e = -\frac{q^2}{\Omega N} \sum_{\varepsilon_{n\mathbf{k}} \geq 0} v_{n\mathbf{k}\alpha} v_{n\mathbf{k}\beta} \tau_{n\mathbf{k}} \frac{\partial f_{n\mathbf{k}}^0}{\partial \varepsilon_{n\mathbf{k}}}, \quad (1.15)$$

$$\sigma_{\alpha\beta}^h = -\frac{q^2}{\Omega N} \sum_{\varepsilon_{n\mathbf{k}} \leq -E_g} v_{n\mathbf{k}\alpha} v_{n\mathbf{k}\beta} \tau_{n\mathbf{k}} \frac{\partial f_{n\mathbf{k}}^0}{\partial \varepsilon_{n\mathbf{k}}}, \quad (1.16)$$

where E_g is the band gap energy. The electron mobility is $\mu_{\alpha\beta}^e = \sigma_{\alpha\beta}^e/ne$ and the hole mobility is $\mu_{\alpha\beta}^h = \sigma_{\alpha\beta}^h/pe$, where n and p are electron concentration and hole concentration, respectively. The total mobility is defined by,

$$\mu_{\alpha\beta} = \frac{\sigma_{\alpha\beta}}{(n+p)e} = \frac{n\mu_{\alpha\beta}^e + p\mu_{\alpha\beta}^h}{n+p}. \quad (1.17)$$

The second term in Eq. 1.11 represents the contribution to the electrical current from the temperature gradient and the tensor \mathbf{L}_{12} writes,

$$L_{\alpha\beta}^{12} = -\frac{q}{\Omega TN} \sum_{n\mathbf{k}} v_{n\mathbf{k}\alpha} v_{n\mathbf{k}\beta} \tau_{n\mathbf{k}} (\varepsilon_{n\mathbf{k}} - \mu) \frac{\partial f_{n\mathbf{k}}^0}{\partial \varepsilon_{n\mathbf{k}}}. \quad (1.18)$$

The Seebeck coefficient tensor is defined by,

$$\mathbf{S} = \mathbf{L}_{11}^{-1} \mathbf{L}_{12}. \quad (1.19)$$

In particular, in isotropic materials, the Seebeck coefficient reads,

$$\begin{aligned} S_\alpha &= \frac{L_\alpha^{12}}{L_\alpha^{11}} \\ &= \frac{1}{qT} \frac{\sum_{n\mathbf{k}} v_{n\mathbf{k}\alpha} v_{n\mathbf{k}\alpha} \tau_{n\mathbf{k}} (\varepsilon_{n\mathbf{k}} - \mu) \frac{\partial f_{n\mathbf{k}}^0}{\partial \varepsilon_{n\mathbf{k}}}}{\sum_{n\mathbf{k}} v_{n\mathbf{k}\alpha} v_{n\mathbf{k}\alpha} \tau_{n\mathbf{k}} \frac{\partial f_{n\mathbf{k}}^0}{\partial \varepsilon_{n\mathbf{k}}}}. \end{aligned} \quad (1.20)$$

Note that the Seebeck coefficient is not an additive quantity thus the accumulated Seebeck coefficient is ill-defined. Nevertheless, we can still define a truncated Seebeck coefficient by changing the condition for the summation both in the numerator and denominator from $\{n\mathbf{k}\}$ to $\{n\mathbf{k}, |\mathbf{v}_{n\mathbf{k}}| \tau_{n\mathbf{k}} < \lambda\}$. Effectively, we are able to calculate the contribution to the Seebeck coefficient of electrons with mean free paths up to a given value λ as,

$$S_\alpha(\lambda) = \frac{1}{qT} \frac{\sum_{l_{n\mathbf{k}} \leq \lambda} v_{n\mathbf{k}\alpha} v_{n\mathbf{k}\alpha} \tau_{n\mathbf{k}} (\varepsilon_{n\mathbf{k}} - \mu) \frac{\partial f_{n\mathbf{k}}^0}{\partial \varepsilon_{n\mathbf{k}}}}{\sum_{l_{n\mathbf{k}} \leq \lambda} v_{n\mathbf{k}\alpha} v_{n\mathbf{k}\alpha} \tau_{n\mathbf{k}} \frac{\partial f_{n\mathbf{k}}^0}{\partial \varepsilon_{n\mathbf{k}}}}. \quad (1.21)$$

The truncated power factor is defined in the same fashion by setting a maximum

mean free path for all summations. The electron and hole Seebeck coefficient are written as

$$S_\alpha^e = \frac{1}{qT} \frac{\sum_{\varepsilon_{n\mathbf{k}} \geq 0} v_{n\mathbf{k}\alpha} v_{n\mathbf{k}\alpha} \tau_{n\mathbf{k}} (\varepsilon_{n\mathbf{k}} - \mu) \frac{\partial f_{n\mathbf{k}}^0}{\partial \varepsilon_{n\mathbf{k}}}}{\sum_{\varepsilon_{n\mathbf{k}} \geq 0} v_{n\mathbf{k}\alpha} v_{n\mathbf{k}\alpha} \tau_{n\mathbf{k}} \frac{\partial f_{n\mathbf{k}}^0}{\partial \varepsilon_{n\mathbf{k}}}}. \quad (1.22)$$

$$S_\alpha^h = \frac{1}{qT} \frac{\sum_{\varepsilon_{n\mathbf{k}} \leq -E_g} v_{n\mathbf{k}\alpha} v_{n\mathbf{k}\alpha} \tau_{n\mathbf{k}} (\varepsilon_{n\mathbf{k}} - \mu) \frac{\partial f_{n\mathbf{k}}^0}{\partial \varepsilon_{n\mathbf{k}}}}{\sum_{\varepsilon_{n\mathbf{k}} \leq -E_g} v_{n\mathbf{k}\alpha} v_{n\mathbf{k}\alpha} \tau_{n\mathbf{k}} \frac{\partial f_{n\mathbf{k}}^0}{\partial \varepsilon_{n\mathbf{k}}}}. \quad (1.23)$$

The first term in Eq. 1.12 corresponds to the heat flow due to the electrochemical potential gradient and the coefficient $\mathbf{L}_{21} = T \mathbf{L}_{12}$. The second term in Eq. 1.12 describes the diffusion of electron under a temperature gradient, where the tensor \mathbf{L}_{22} is defined as,

$$L_{\alpha\beta}^{22} = -\frac{1}{\Omega TN} \sum_{n\mathbf{k}} v_{n\mathbf{k}\alpha} v_{n\mathbf{k}\beta} \tau_{n\mathbf{k}} (\varepsilon_{n\mathbf{k}} - \mu)^2 \frac{\partial f_{n\mathbf{k}}^0}{\partial \varepsilon_{n\mathbf{k}}}. \quad (1.24)$$

Denote the electrochemical potential as $\varphi = \Phi/q$ and the electrical current by electrons and holes are,

$$\mathbf{J}_c^e = -\boldsymbol{\sigma}^e \cdot \nabla_{\mathbf{r}} \varphi - \boldsymbol{\sigma}^e \cdot \mathbf{S}^e \cdot \nabla_{\mathbf{r}} T, \quad (1.25)$$

$$\mathbf{J}_c^h = -\boldsymbol{\sigma}^h \cdot \nabla_{\mathbf{r}} \varphi - \boldsymbol{\sigma}^h \cdot \mathbf{S}^h \cdot \nabla_{\mathbf{r}} T, \quad (1.26)$$

and separated energy flux by electrons and holes are,

$$\begin{aligned} \mathbf{J}^e &= -T \boldsymbol{\sigma}^e \cdot \mathbf{S}^e \cdot \nabla_{\mathbf{r}} \varphi - \mathbf{L}_{22}^e \cdot \nabla_{\mathbf{r}} T \\ &= T \boldsymbol{\sigma}^e \cdot \mathbf{S}^e \cdot (\boldsymbol{\sigma}^e)^{-1} \cdot \mathbf{J}_c^e - [\mathbf{L}_{21}^e (\mathbf{L}_{11}^e)^{-1} \mathbf{L}_{12}^e + \mathbf{L}_{22}^e] \cdot \nabla_{\mathbf{r}} T, \end{aligned} \quad (1.27)$$

$$\begin{aligned} \mathbf{J}^h &= -T \boldsymbol{\sigma}^h \cdot \mathbf{S}^h \cdot \nabla_{\mathbf{r}} \varphi - \mathbf{L}_{22}^h \cdot \nabla_{\mathbf{r}} T \\ &= T \boldsymbol{\sigma}^h \cdot \mathbf{S}^h \cdot (\boldsymbol{\sigma}^h)^{-1} \cdot \mathbf{J}_c^h - [\mathbf{L}_{21}^h (\mathbf{L}_{11}^h)^{-1} \mathbf{L}_{12}^h + \mathbf{L}_{22}^h] \cdot \nabla_{\mathbf{r}} T. \end{aligned} \quad (1.28)$$

We then know the electronic thermal conductivity tensor $\boldsymbol{\kappa}_e$ is given by,

$$\boldsymbol{\kappa}_e = \mathbf{L}_{22} - \mathbf{L}_{21} \mathbf{L}_{11}^{-1} \mathbf{L}_{12}. \quad (1.29)$$

The electrical thermal conductivity defined by Eq. 1.29 does not include the heat conduction due to ambipolar diffusion. At high temperatures, electrons can be thermally excited from valence band to the conduction band. Such process absorbs heat and its

inverse process releases heat. The temperature gradient in thermoelectric materials leads to spatial dependent electron-hole pair generation/recombination processes. In this fashion, the heat can be migrated from the hot side to the cold side even though net electrical current is zero. Let the net current to be zero $\mathbf{J}_c = \mathbf{J}_c^e + \mathbf{J}_c^h = 0$ and plug it in Eq. 1.25 and Eq. 1.26. We have $\nabla_{\mathbf{r}}\varphi = -(\boldsymbol{\sigma}^e + \boldsymbol{\sigma}^h)^{-1} \cdot (\boldsymbol{\sigma}^e \cdot \mathbf{S}^e + \boldsymbol{\sigma}^h \cdot \mathbf{S}^h) \cdot \nabla_{\mathbf{r}}T$. Then, we rewrite the electrical current as,

$$\mathbf{J}_c^e = -\mathbf{J}_h^e = \left[\boldsymbol{\sigma}^e \cdot (\boldsymbol{\sigma}^e + \boldsymbol{\sigma}^h)^{-1} \cdot \boldsymbol{\sigma}^h \cdot \mathbf{S}^h - \boldsymbol{\sigma}^h \cdot (\boldsymbol{\sigma}^e + \boldsymbol{\sigma}^h)^{-1} \cdot \boldsymbol{\sigma}^e \cdot \mathbf{S}^e \right] \cdot \nabla_{\mathbf{r}}T. \quad (1.30)$$

Plug the electrical current into the heat flux equation in Eq. 1.27 and Eq. 1.28,

$$\begin{aligned} \mathbf{J}_c &= T\boldsymbol{\sigma}^e \cdot \mathbf{S}^e \cdot (\boldsymbol{\sigma}^e)^{-1} \cdot \mathbf{J}_c^e - \boldsymbol{\kappa}_e^e \cdot \nabla_{\mathbf{r}}T, \\ \mathbf{J}_h &= T\boldsymbol{\sigma}^h \cdot \mathbf{S}^h \cdot (\boldsymbol{\sigma}^h)^{-1} \cdot \mathbf{J}_c^h - \boldsymbol{\kappa}_e^h \cdot \nabla_{\mathbf{r}}T, \\ \mathbf{J} &= \mathbf{J}^e + \mathbf{J}^h \\ &= - \left[-\mathbf{L}_{21}^e \mathbf{L}_{11}^{-1} \mathbf{L}_{12}^h + \mathbf{L}_{21}^e \boldsymbol{\sigma}_e^{-1} \boldsymbol{\sigma}_h \mathbf{L}_{11}^{-1} \mathbf{L}_{12}^e - \mathbf{L}_{21}^h \mathbf{L}_{11}^{-1} \mathbf{L}_{12}^e + \mathbf{L}_{21}^h \boldsymbol{\sigma}_h^{-1} \boldsymbol{\sigma}_e \mathbf{L}_{11}^{-1} \mathbf{L}_{12}^h \right] \cdot \nabla_{\mathbf{r}}T \\ &\quad - \boldsymbol{\kappa}_e^e \cdot \nabla_{\mathbf{r}}T - \boldsymbol{\kappa}_e^h \cdot \nabla_{\mathbf{r}}T. \end{aligned} \quad (1.31)$$

This is equivalent to cases of the heat conduction by electrons and holes in an open-circuit thermoelectric leg subject to a temperature gradient where there is zero current but finite voltage difference and heat flux. The first term is the bipolar thermal conductivity tensor,

$$\boldsymbol{\kappa}^{bp} = (\mathbf{L}_{21}^e \boldsymbol{\sigma}_e^{-1} \boldsymbol{\sigma}_h - \mathbf{L}_{21}^h) \mathbf{L}_{11}^{-1} \mathbf{L}_{12}^e + (\mathbf{L}_{21}^h \boldsymbol{\sigma}_h^{-1} \boldsymbol{\sigma}_e - \mathbf{L}_{21}^e) \mathbf{L}_{11}^{-1} \mathbf{L}_{12}^h. \quad (1.32)$$

In isotropic materials, it reduces to,

$$\kappa_{\alpha}^{bp} = \frac{\sigma_{\alpha}^e \sigma_{\alpha}^h}{\sigma_{\alpha}^e + \sigma_{\alpha}^h} (S_{\alpha}^e - S_{\alpha}^h)^2 T. \quad (1.33)$$

1.3 Electron scattering rate

In the previous section, we have derived the linearized Boltzmann transport equation with relaxation time approximation,

$$\frac{df_{n\mathbf{k}}}{dt} \Big|_{\text{coll}} = -\frac{f_{n\mathbf{k}} - f_{n\mathbf{k}}^0}{\tau_{n\mathbf{k}}}. \quad (1.34)$$

Since generally the collision term $\frac{df_{n\mathbf{k}}}{dt} \Big|_{\text{coll}}$ involves all distribution $f_{n\mathbf{k}'}$, such approximation requires justification, especially in polar materials where the optical phonon energy is relatively higher. A specific formalism to solve the Boltzmann transport equation beyond relaxation time approximation is the iterative solver, which will be discussed in Chapter 3. Nevertheless, the lifetime $\tau_{n\mathbf{k}}$ is generally a good physical quantity to describe electron dynamics. As electron is constantly scattered through various scattering mechanisms, it is usually assumed that the total electron scattering rate is the sum of all individual types of scattering, known as the *Matthiessen's rule*,

$$\frac{1}{\tau_{n\mathbf{k}}} = \sum_i \frac{1}{\tau_{n\mathbf{k},i}}. \quad (1.35)$$

In the following part, we will present typical scattering mechanisms for semiconductors.

Interaction with acoustic phonons. Acoustic phonons are believed to be primarily responsible for the scattering of electrons in non-polar materials. In 1950, Bardeen and Shockley proposed the idea of deformation potential to explain the mobility in solids[3]. In their picture, the energy bands are gradually shifted resulting from the local deformation of the lattice due to phonon. Based on the Fermi's Golden Rule, the scattering rate is,

$$S(n\mathbf{k}, m\mathbf{k}') = \frac{2\pi}{\hbar} |\langle n\mathbf{k}|U|m\mathbf{k}'\rangle|^2 \delta(\varepsilon_{m\mathbf{k}'} - \varepsilon_{n\mathbf{k}} - \Delta\varepsilon) f_{n\mathbf{k}}(1 - f_{m\mathbf{k}}), \quad (1.36)$$

where $\Delta\varepsilon$ is the energy transfer through the scattering event and U is the perturbed

potential. The perturbed potential due to deformation of an acoustic phonon writes,

$$U(x, t) = D_A \frac{\partial u(x, t)}{\partial x}, \quad (1.37)$$

where D_A is the deformation potential constant, and u is the displacement of the ion. The acoustic wave is usually described by,

$$u = A_k e^{i(kx - \omega t)} + c.c. \quad (1.38)$$

The scattering rate due to acoustic deformation phonon scattering is,

$$\frac{1}{\tau_{n\mathbf{k}, \text{ADP}}} = \sum_{m\mathbf{k}'} S(n\mathbf{k}, m\mathbf{k}') \quad (1.39)$$

In a parabolic band model, the scattering rate reads,

$$\frac{1}{\tau_{n\mathbf{k}, \text{ADP}}} = \frac{D_A^2 k_B T (2m_d^*)^{3/2} \varepsilon_{n\mathbf{k}}^{1/2}}{2\pi\hbar^4 C_l}, \quad (1.40)$$

where C_l is the average longitudinal elastic modulus and m_d^* is the single-valley density-of-state effective mass.

Interaction with non-polar optical phonons. For optical phonons, the perturbed potential is due to the opposite displacement (out of phase) of the ions. The lattice spacing is directly related to the displacement, which leads to the perturbed potential,

$$U(x, t) = D_O u(x, t) \quad (1.41)$$

For simplicity, we can neglect the variance of the optical phonon. If the optical phonon frequency is denoted by ω_o , the scattering rate due to non-polar optical deformation potential scattering is,

$$\frac{1}{\tau_{n\mathbf{k}, \text{ODP}}} = \frac{\pi D_O^2 k_B T (2m_d^*)^{3/2} \varepsilon_{n\mathbf{k}}^{1/2}}{2\hbar^2 a^2 \rho (\hbar\omega_o)^2} \quad (1.42)$$

where a is the lattice constant and ρ is the density.

Interaction with polar optical phonons. For a material with more than two kinds of ions, the charge associated with each ion is different. The optical phonon not only deforms the lattice but creates polarization. For a long-wavelength optical phonon, in different unit cells, the ion displacements as well as the dipoles are similar, which means that the polarization can be significant. In another word, the interaction between the electron and the long-wavelength polar optical modes can be significant. This is known as the polarization scattering or polar scattering. In gallium arsenide (GaAs), for example, the major scattering mechanism for electrons is believed to be polar scattering.

For a unit cell with ions associated with different charges, the relative displacements of the positively charged ion to the negatively charged ion is,

$$\begin{aligned} & \frac{1}{Q} \left(\sum_{\alpha} e_{\alpha} \Delta R_{\alpha} - \sum_{\beta} |e_{\beta}| \Delta R_{\beta} \right) \\ &= \frac{1}{\sqrt{N}} \left(\frac{\hbar}{2M_{\nu\mathbf{q}}\omega_{\nu\mathbf{q}}} \right)^{1/2} \times [u_{\nu\mathbf{q}} a_{\nu\mathbf{q}}^+ e^{i\mathbf{q}\cdot\mathbf{R}} - u_{\nu\mathbf{q}}^* a_{\nu\mathbf{q}} e^{-i\mathbf{q}\cdot\mathbf{R}}], \end{aligned} \quad (1.43)$$

where \mathbf{R} is the lattice site, $e_{\alpha/\beta}$ is the number of charge associated with positively/negatively charged ion and $Q = \sum_{\alpha} e_{\alpha} = \sum_{\beta} |e_{\beta}|$. The displacement due to phonon mode $\nu\mathbf{q}$ satisfies,

$$\begin{aligned} d_{\nu\mathbf{q}} &= \frac{\mathbf{u}_{\nu\mathbf{q}}}{M_{\nu\mathbf{q}}^{1/2}} = \frac{1}{Q} \left[\sum_{\alpha} \frac{e_{\alpha} \mathbf{e}_{\nu\mathbf{q}\alpha}}{M_{\alpha}^{1/2}} - \sum_{\beta} \frac{|e_{\beta}| \mathbf{e}_{\nu\mathbf{q}\beta}}{M_{\beta}^{1/2}} \right], \\ \frac{\mathbf{e}_{\nu\mathbf{q}}}{M_{\nu\mathbf{q}}^{1/2}} &= \frac{1}{n} \sum_i^n \frac{\mathbf{e}_{\nu\mathbf{q}i}}{M_i^{1/2}}, \end{aligned} \quad (1.44)$$

where M_i is the mass of i th ion, $\mathbf{e}_{\nu\mathbf{q}}$ is the eigenvector of the phonon mode $\nu\mathbf{q}$ and $\mathbf{e}_{\nu\mathbf{q}i}$ is the eigenvector of i th ion. The electrical field due to the relative displacement is,

$$E_{\nu\mathbf{q}} = -4\pi e_{\nu\mathbf{q}}^* \mathbf{d}_{\nu\mathbf{q}} \cdot \frac{\mathbf{q}}{|\mathbf{q}|}, \quad (1.45)$$

where the effective charge is defined by $e_{\nu\mathbf{q}}^* = M_{\nu\mathbf{q}}^{1/2} \sqrt{\frac{\omega_0^2}{4\pi} \left(\frac{1}{\epsilon_{\infty}} - \frac{1}{\epsilon_0} \right)}$. The polar scat-

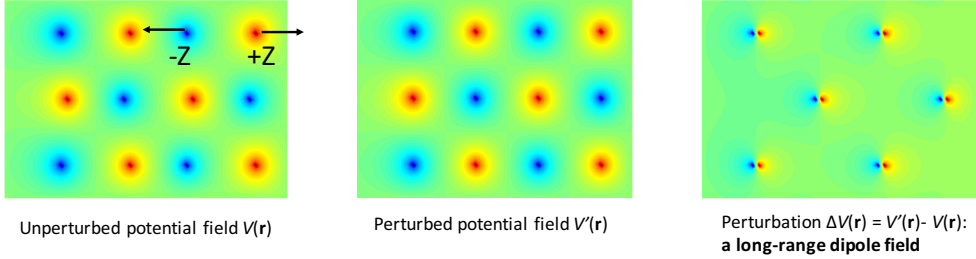


Figure 1-1: The origin of the long-range dipole field due to LO phonon in polar material consisting two atoms per unit cell.

tering rate is written as[41],

$$\frac{1}{\tau_{n\mathbf{k},PO}} = \frac{e^2 \omega_o (\epsilon_\infty^{-1} - \epsilon_0^{-1})}{h \sqrt{2\varepsilon_{n\mathbf{k}}/m_d^*}} \left[N_o \sinh^{-1} \left(\frac{\varepsilon_{n\mathbf{k}}}{\hbar\omega_o} \right)^{1/2} + (N_o + 1) \sinh^{-1} \left(\frac{\varepsilon_{n\mathbf{k}}}{\hbar\omega_o} - 1 \right)^{1/2} \right] \quad (1.46)$$

where N_o is the population of the longitudinal optical phonon.

1.4 A brief review of previous computational work

A full calculation of the thermoelectric transport properties using first principles is useful because it can provide insights, such as the electro/hole mean free paths, for experimentalists to optimize the thermoelectric performance of the materials. Such calculation is complicated as it is involved with numerous interdependent material parameters. Some intrinsic material parameters are difficult to extract from experiments, *e.g.* the lifetime of electrons. Previous computational works has to adopt certain level of assumptions to make the calculation of the transport properties.

Constant relaxation time approximation. In Eq. 1.20, the lifetime of the carrier appears in the numerator and the denominator at the same time, implying that the Seebeck coefficient might not be sensitive to the carrier lifetime given a weak enough dependence of lifetime on the wavevector. The electrical conductivity is closely related to the carrier lifetime. The simplest treatment is to neglect the k -dependence of the carrier lifetime. A successful computational formalism named as BoltzTrap developed by Madsen and Singh[43] assumes a constant relaxation time for all carri-

ers and compute the transport properties based on the band structures from density functional theory (DFT) on a highly dense k -point mesh. It turned out to be a good approximation for highly-doped semiconductors. For example, the Seebeck coefficient of PbTe from calculation agrees well with experiments for different doping concentrations[64]. Based on results from such type of calculation, people also attributed the high Seebeck coefficient and high mobility of PbTe at the same time to the strongly corrugated shape of isoenergy surfaces[9].

The band structure calculation does not require a lot of computation resource, making it possible to do a high-throughput calculation for various thermoelectric materials[24]. The disadvantage of this approach is that one has to assign a value for the lifetime to calculate the electrical conductivity. To the best of our knowledge, there is no report of first-principles calculation of the carrier lifetime in PbTe.

Band structures beyond DFT at zero Kelvin. Considering the fact that the band gap rendered by DFT calculation is often underestimated, calculation beyond DFT could potentially improve the accuracy of the BoltzTrap calculation. In addition, the doping[18] and finite temperature could both modify the band structures thus the band structure from zero-Kelvin DFT calculation does not seem to be plausible. Svane *et al.* applied quasiparticle self-consistent GW calculation to calculate the band gap and effective mass and achieved good agreement with experiments[68]. Gibbs *et al.* showed through ab initio molecular dynamics calculation in a supercell that the light band at L point and heavy band at Σ point converge at 700 K, consistent with optical measurements of the band gap. In 2014, Skelton *et al.* investigated the temperature effects on the band structures by giving specific lattice constants predicted using quasi-harmonic approximation (QHA)[65]. Although for each calculation, it is still zero-Kelvin calculation, they were able to obtain a more accurate band structure at finite temperatures.

Corrected $\mathbf{k} \cdot \mathbf{p}$ scheme for accurate band structures. The GW calculation of band structures is believed to be more accurate than DFT, yet the dramatically increased computational cost makes the computation on a fine k mesh unachievable. In 2017, Berland *et al.* proposed a corrected scheme by solving the $\mathbf{k} \cdot \mathbf{p}$ method and extrapo-

lating the band structures from several k points[5]. They demonstrate that not only the band structures, but the density of states as well as dielectric constant can be accurately extrapolated with computational cost on a sparse grid.

Fully first-principle calculation of electron transport in Si and GaAs. In 2015, Qiu *et al.* carried out the fully first-principle electron transport in silicon[58]. The electron-phonon scattering rate was calculated using electron-phonon Wannier interpolation based on maximally localized Wannier functions and the electron mean free paths are reported. Unlike in non-polar silicon, the polarization scattering for electron can be significant in polar materials. In 2017, Liu *et al.* calculated the intrinsic electron lifetime in GaAs within the relaxation time approximation[40]. They also calculated the electron mobility iteratively, achieving great agreements with experimental results. In practical thermoelectric materials, the *ab initio* calculation of electron transport is more complicated. For PbTe, it is known that the strong spin-orbit coupling leads to non-parabolic band structure, which requires a fully-relativistic calculation. Also, the screening effect of free carriers that affects the polar scattering should be considered.

1.5 Outline of the thesis

The goal of the thesis is to go beyond the constant relaxation time approximation and calculate the electron-phonon interaction rigorously. In Chapter 1, we have briefly reviewed previous computational efforts in calculating electrical transport properties using *ab initio* method. In Chapter 2, we first compactly introduce key assumptions in DFT. We review the density functional perturbation theory (DFPT) for the lattice dynamics calculation. In Chapter 3, we introduce the electron-phonon Wannier interpolation scheme to calculate the electron-phonon coupling matrix on a very fine grid. In Chapter 4, we present the *ab initio* electron mean free paths, electron transport properties and phonon transport properties in *n*-type PbTe. In Chapter 5, we summarize the findings and wisdom provided by calculation, and identify the future direction.

Chapter 2

Lattice dynamics from first principles

The density functional theory provides a parameter-free way towards the ground states of a electronic system. Phonon is considered as a perturbation to the ground states due to atom displacement. The $2n+1$ theorem states that the $(2n+1)th$ derivative of the eigenvalue of a Hamiltonian can be calculated with only the knowledge of the variance in the eigenfunctions up to order n [30]. In the sprit of $2n+1$ theorem, the *density functional perturbation theory (DFPT)* was proposed by Baroni[4] and Gonze[22] to calculate the phonon properties (first order) only requiring zeroth-order wavefunctions. In DFPT, the responses to perturbation is obtained by computing the system subject to external potential within the DFT formalism.

2.1 Density functional theory

Due to large mass difference between the ion and the electron, the Born-Oppenheimer approximation is considered to be a reasonable approximation to simplify the Schrödinger equation. Whenever the ion moves, the electron responds fast enough such that the ion is considered as fixed. This approximation allows us to construct the wavefunction as $\Phi = \phi_{\text{electron}} \times \phi_{\text{nuclei}}$. The correlated nature of electrons in solids makes it impossible to solve the many-body Schrödinger equation directly. A certain level of approximation needs to be adopted to obtain the electron eigenstates in the solids. The Hohenberg-Kohn theorem provides a new perspective to construct the equation

of motion for electrons in solids:

- *Theorem 1* The external potential and the total energy is a unique functional of electron density $\rho(\mathbf{r})$.
- *Theorem 2* The ground state energy can be obtained variationally and the density that minimizes the total energy is the exact ground state density.

For a very long time, scientists had struggled to find that functional of density. Eventually, some approximated form of the functional is shown to be able to simplify the many-body Schrödinger equation to a set of one-electron equations and the reproduce the correct material properties.

2.1.1 Hartree approximation

The Hartree approximation states that the *ansatz* for the many-body electron wavefunction may write as,

$$\Phi(\mathbf{r}_1, \mathbf{r}_2, \dots, \mathbf{r}_N) = \phi(\mathbf{r}_1)\phi(\mathbf{r}_2)\cdots\phi(\mathbf{r}_N). \quad (2.1)$$

Each particle is regarded as independent and interacts with each other through the mean-field Coulomb potential. The corresponding Schrödinger equation is,

$$\left[-\frac{\hbar^2}{2m} \nabla^2 + V(\mathbf{r}) \right] \phi_i(\mathbf{r}) = \varepsilon_i \phi_i(\mathbf{r}), \quad (2.2)$$

where m is the electron mass. The potential has two parts, the electron-nucleus interaction and electron-electron interaction, both in the form of Coulomb potential,

$$V(\mathbf{r}) = -Ze^2 \sum_{\mathbf{R}} \frac{1}{4\pi\epsilon_0 |\mathbf{r} - \mathbf{R}|} - e^2 \int d\mathbf{r}' \rho(\mathbf{r}') \frac{1}{4\pi\epsilon_0 |\mathbf{r} - \mathbf{r}'|}, \quad (2.3)$$

where Z is the charge of the ion and ϵ_0 is the permittivity of free space.

2.1.2 Hartree-Fock approximation

The Hartree approximation fails to capture the exchange interaction. The exchange interaction is due to the *Pauli exclusion principle*, which leads to antisymmetry when exchanging particle,

$$\Phi(\mathbf{x}_1, \mathbf{x}_2, \dots, \mathbf{x}_i, \dots, \mathbf{x}_j, \dots, \mathbf{x}_N) = -\Phi(\mathbf{x}_1, \mathbf{x}_2, \dots, \mathbf{x}_j, \dots, \mathbf{x}_i, \dots, \mathbf{x}_N), \quad (2.4)$$

where \mathbf{x}_i is the coordinate that includes position and spin. To satisfy such permutation symmetry, one generalized form of the solution to the wavefunction is the *Slater determinant*,

$$\Phi(\mathbf{x}_1, \mathbf{x}_2, \dots, \mathbf{x}_N) = \frac{1}{\sqrt{N!}} \begin{vmatrix} \phi_1(\mathbf{x}_1) & \phi_2(\mathbf{x}_1) & \dots & \phi_N(\mathbf{x}_1) \\ \phi_1(\mathbf{x}_2) & \phi_2(\mathbf{x}_2) & \dots & \phi_N(\mathbf{x}_2) \\ \vdots & \vdots & \ddots & \vdots \\ \phi_1(\mathbf{x}_N) & \phi_2(\mathbf{x}_N) & \dots & \phi_N(\mathbf{x}_N) \end{vmatrix}. \quad (2.5)$$

This leads the following Schrödinger equation, also known as the Hartree-Fock equation,

$$\left(-\frac{\hbar^2}{2m} \nabla^2 - Ze^2 \sum_{\mathbf{R}} \frac{1}{4\pi\epsilon_0 |\mathbf{r} - \mathbf{R}|} - \sum_j e^2 \int d\mathbf{r}' \frac{|\phi_j(\mathbf{r}')|^2}{4\pi\epsilon_0 |\mathbf{r} - \mathbf{r}'|} \right) \phi_i(\mathbf{r}) - \sum_j \delta_{s_i, s_j} e^2 \int d\mathbf{r}' \frac{\phi_j^*(\mathbf{r}') \phi_i(\mathbf{r}')}{4\pi\epsilon_0 |\mathbf{r} - \mathbf{r}'|} \phi_i(\mathbf{r}) = \varepsilon_i \phi_i(\mathbf{r}) \quad (2.6)$$

where $\phi_j^*(\mathbf{r}')$ is the complex conjugate of $\phi_j(\mathbf{r}')$ and s_i is the spin of the electron. The last term in Eq. 2.6 describes the exchange interaction. However, the exchange term is a non-local operator for ϕ_i making the Hartree-Fock equation difficult to solve in big systems such as periodic solids.

2.1.3 Kohn-Sham equation, local density approximation and pseudopotentials

The Hartree-Fock equation include the exchange interaction, yet the correlation interaction is missed, which describes the influence on the movement of one electron by the presence of all other electrons. The key to resolve the issue is to modified the form of the effective potential. In 1965, Walter Kohn and Lu Jeu Sham[32] proposed a new way to include exchange-correlation interaction,

$$\left[-\frac{\hbar^2}{2m} \nabla^2 + V_{\text{eff}}(\mathbf{r}) \right] \phi_i(\mathbf{r}) = \varepsilon_i \phi_i(\mathbf{r}). \quad (2.7)$$

The effective potential reads,

$$V_{\text{eff}}(\mathbf{r}) = V_{\text{ext}}(\mathbf{r}) + e^2 \int d\mathbf{r}' \frac{\rho(\mathbf{r}')}{4\pi\epsilon_0 |\mathbf{r} - \mathbf{r}'|} + \frac{\delta E_{\text{xc}}[\rho]}{\delta \rho(\mathbf{r})}, \quad (2.8)$$

where charge density $\rho(\mathbf{r}) = \sum_i |\phi_i(\mathbf{r})|^2$ and the last term is the exchange-correlation potential. Later, the local-density approximation is proposed to provide a way to construct the exchange-correlation potential. In spin-unpolarized system, the exchange-correlation energy writes,

$$E_{\text{xc}}[\rho] = \int d\mathbf{r} \rho(\mathbf{r}) \varepsilon_{\text{xc}}(\rho), \quad (2.9)$$

where ε_{xc} the exchange-correlation energy per particle of a homogeneous electron gas with charge density $\rho(\mathbf{r})$. The potential due to core valence electrons is included in $V_{\text{ext}}(\mathbf{r})$. The core is usually regarded as independent of the environment and can be substituted by a pseudopotential. The pseudopotential replaces the Coulomb electron-ionic core interactions and it consists long-ranged local part and short-ranged non-local part,

$$V_i = V_{nl} + V_{loc}, \quad (2.10)$$

where i represents i th ion. The long-ranged local part at a large distance to the ion center returns to the trivial Coulomb potential. Conversely, the short-ranged non-local part is written in terms of the sum of several angular-momentum dependent

potentials within the LDA,

$$V_{loc}(\mathbf{r}) = \sum_l V_l(r) |l\rangle \langle l|. \quad (2.11)$$

In practice, the non-local pseudopotentials are written as a semilocal operator,

$$\hat{V}_{sl} = \sum_{lm} V_l(r) \delta(r - r') Y_{lm}(\hat{\mathbf{r}}) Y_{lm}^*(\hat{\mathbf{r}'}) \quad (2.12)$$

where Y_{lm} is the spherical harmonic function of degree l and order m defined in spherical harmonics.

To be more specific, we carried out the first-principles calculation on electronic band structure using a $6 \times 6 \times 6$ Monkhorst-Pack[50] k -grid with the cutoff energy of 70 Ry. We choose the norm-conserving fully relativistic pseudopotentials with local density approximation (LDA) for exchange-correlation energy functional. The calculation includes the spin-orbit coupling, implemented in Quantum ESPRESSO package[16]. The lattice constant used in calculation is 6.29 Å. The band gap given by the DFT calculation is 0.15 eV. As is known, the DFT-LDA suffers from underestimating the material's band gap. This is because the LDA has erroneous self-interaction: the exact exchange-correlation energy functional should cancel the self-interaction yet LDA does not. The LDA tends to over-delocalize the occupied states, leading to a higher energy of those states thus a smaller band gap[72]. In our case, we rigidly shift the conduction bands to match the band gap at room temperature, which is 0.316 eV[59]. The doping is modeled with a rigid band model approximation and dopants are assumed to be fully ionized in the whole temperature range in the calculation. Given the number of dopants, the chemical potential is obtained by solving the charge neutrality equation.

We would also like to address the effect of temperature on the band structure. There are several ways to calculate the band structure considering the temperature effect. The most straightforward way is the *ab initio* molecular dynamics[17]. We adopt the temperature-dependent band gap from experiment[59] and compare the

results with constant-band-gap calculation. We realize that the difference between the two cases is insignificant[1]. Consequently, we apply the same lattice constant and band gap for all calculations and the temperature effect is encoded in the distribution functions of electrons and phonons.

2.2 Density functional perturbation theory

The density functional theory provides a way to obtain the ground state energy. Based on linear response theory, the lattice vibration can be also studied by the density functional theory. The density functional-perturbation theory is the *ab initio* theory of lattice vibrations. Within the Born-Oppenheimer approximation, the Schrödinger equation that describes the lattice dynamics is,

$$\left[-\sum_i \frac{\hbar^2}{2M_i} \frac{\partial^2}{\partial \mathbf{R}_i^2} + E(\mathbf{R}) \right] \Phi_{\text{ion}}(\mathbf{R}) = \varepsilon \Phi_{\text{ion}}(\mathbf{R}), \quad (2.13)$$

where M_i is the i th ion mass and \mathbf{R}_i is the position of its position. The $E(\mathbf{R})$ is the clamped-ion energy of the system composed of ion with fixed position and interacting electrons. The Hamiltonian to describe such system writes (in atomic unit),

$$H_{\text{BO}}(\mathbf{R}) = -\frac{\hbar^2}{2m} \sum_k \frac{\partial^2}{\partial \mathbf{r}_k^2} + \frac{e^2}{2} \sum_{k \neq j} \frac{1}{|\mathbf{r}_k - \mathbf{r}_j|} - \sum_{ik} \frac{Z_i e^2}{|\mathbf{r}_k - \mathbf{R}_i|} + \frac{e^2}{2} \sum_{i \neq l} \frac{Z_i Z_l}{|\mathbf{R}_i - \mathbf{R}_l|}. \quad (2.14)$$

The Hessian matrix scaled by the nuclear masses is,

$$\mathbf{M} = \frac{1}{\sqrt{M_i M_j}} \frac{\partial^2 E(\mathbf{R})}{\partial \mathbf{R}_i \partial \mathbf{R}_j}. \quad (2.15)$$

And the phonon frequency is the eigenvalue of the Hessian matrix by,

$$\det \left| \mathbf{M} - \omega^2 \right| = 0 \quad (2.16)$$

To obtain the force, we refer to the Hellmann-Feynman theorem which states,

$$\frac{\partial E_\lambda}{\partial \lambda} = \left\langle \Psi_\lambda \left| \frac{\partial H_\lambda}{\partial \lambda} \right| \Psi_\lambda \right\rangle, \quad (2.17)$$

where Ψ_λ is the eigenfunction of the Hamiltonian and λ is a parameter. Letting the λ to be the position \mathbf{r} , we find that the force acting on i th nucleus is determined by,

$$\mathbf{F}_i = -\frac{\partial E(\mathbf{R})}{\partial \mathbf{R}_i} = \left\langle \Psi(\mathbf{R}) \left| -\frac{\partial H_{\text{BO}}}{\partial \mathbf{R}_i} \right| \Psi(\mathbf{R}) \right\rangle. \quad (2.18)$$

Then, the Hessian is represented by,

$$\frac{\partial^2 E(\mathbf{R})}{\partial \mathbf{R}_i \partial \mathbf{R}_j} = -\frac{\partial \mathbf{F}_i}{\partial \mathbf{R}_j}. \quad (2.19)$$

2.2.1 Linear response theory

The essence of linear response theory is the transfer function that correlates the input and the output. In the case of lattice dynamics, the transfer function is the interatomic force constant that describes the energy variance upon atom displacement. In the realm of density functional theory, the perturbation due to atom displacement can be represented by the charge density. Based on the Hellmann-Feynman theorem, the first and seconder derivatives of the energy can be written as,

$$\begin{aligned} \frac{\partial E}{\partial \lambda_i} &= \int \frac{\partial V_\lambda(\rho)}{\partial \lambda_i} \rho_\lambda(\mathbf{r}) d\mathbf{r}, \\ \frac{\partial^2 E}{\partial \lambda_i \partial \lambda_j} &= \int \frac{\partial^2 V_\lambda(\mathbf{r})}{\partial \lambda_i \partial \lambda_j} \rho_\lambda(\mathbf{r}) d\mathbf{r} + \int \frac{\partial \rho_\lambda(\mathbf{r})}{\partial \lambda_i} \frac{\partial V_\lambda(\mathbf{r})}{\partial \lambda_j} d\mathbf{r}. \end{aligned} \quad (2.20)$$

To calculate the force constant, the parameter λ is the position of the atom \mathbf{R} . In the density functional theory formalism, the effective potential is also called self-consistent field (SCF) potential,

$$V_{\text{SCF}} = V_{\text{ext}}(\mathbf{r}) + e^2 \int d\mathbf{r}' \frac{\rho(\mathbf{r}')}{|\mathbf{r} - \mathbf{r}'|} + v_{\text{xc}}(\mathbf{r}). \quad (2.21)$$

2.2.2 General form of perturbed potential

Upon the perturbation, the perturbed potential to the lowest order is,

$$\Delta V_{\text{SCF}}(\mathbf{r}) = \Delta V_{\text{ext}}(\mathbf{r}) + e^2 \int d\mathbf{r}' \frac{\Delta\rho(\mathbf{r}')}{|\mathbf{r} - \mathbf{r}'|} + \left. \frac{dv_{xc}(\rho)}{d\rho} \right|_{\rho=\rho(\mathbf{r})} \Delta\rho(\mathbf{r}). \quad (2.22)$$

The lowest-order perturbed part of the eigenfunction is given by,

$$\Delta\psi_n(\mathbf{r}) = \sum_{m \neq n} \psi_m(\mathbf{r}) \frac{\langle \psi_m | \Delta V_{\text{SCF}} | \psi_n \rangle}{\varepsilon_n - \varepsilon_m}. \quad (2.23)$$

The corresponding perturbed part of the charge density is,

$$\Delta\rho(\mathbf{r}) = 4 \sum_{n=1}^{N/2} \sum_{m \neq n} \psi_n^*(\mathbf{r}) \phi_m(\mathbf{r}) \frac{\langle \psi_m | \Delta V_{\text{SCF}} | \psi_n \rangle}{\varepsilon_n - \varepsilon_m}. \quad (2.24)$$

2.3 Phonons in polar materials

We have shown the force constant based on perturbation theory in first principles. To study phonons distinguished by wavevector and polarization, in particular, phonon dispersion, we need to construct the corresponding physical quantities in the reciprocal space. Consider the Fourier transform of Eq. 2.22,

$$\Delta V_{\text{SCF}}(\mathbf{q}) = \frac{1}{V} \int \Delta V_{\text{SCF}}(\mathbf{r}) e^{-i\mathbf{q}\cdot\mathbf{r}} d\mathbf{r} = \Delta V(\mathbf{q}) + \frac{4\pi e^2}{q^2} \Delta n(\mathbf{q}) + \frac{dv_{xc}}{dn} \Delta n(\mathbf{q}). \quad (2.25)$$

This is a generalized perturbation potential as a function of wavevector q . We also need to obtain the force constant in the reciprocal space. If the position of i th atom is,

$$\mathbf{R}_i = \mathbf{R}_l + \boldsymbol{\tau}_s + \mathbf{u}_s(l), \quad (2.26)$$

where \mathbf{R}_l is l th lattice site, $\boldsymbol{\tau}_s$ is the equilibrium position of s th atom relative to l th lattice site and $\mathbf{u}_s(l)$ is the deviation of the s th atom from its equilibrium.

Based on Eq. 2.19, the force constant involved with the displacements of i th and

j th atom is,

$$C_{st}^{\alpha\beta}(l, m) = \frac{\partial^2 E}{\partial u_s^\alpha(l) \partial u_t^\beta(m)} = C_{st}^{\alpha\beta}(\mathbf{R}_l, \mathbf{R}_m). \quad (2.27)$$

The Fourier transform of the force constant reads,

$$\tilde{C}_{st}^{\alpha\beta}(\mathbf{q}) = \sum_R e^{-i\mathbf{q}\cdot\mathbf{R}} C_{st}^{\alpha\beta}(\mathbf{R}), \quad (2.28)$$

where we take advantage of the translational symmetry and simplify the real-space force constant to be $C_{st}^{\alpha\beta}(\mathbf{R}_l, \mathbf{R}_m) = C_{st}^{\alpha\beta}(\mathbf{R})$. The phonon eigenfrequencies are obtained by solving the equation,

$$\det \left| \frac{1}{\sqrt{M_s M_t}} \tilde{C}_{st}^{\alpha\beta}(\mathbf{q}) - \omega^2(\mathbf{q}) \right| = 0. \quad (2.29)$$

In polar materials, the long-range polarization field as described by Eq. 1.43 leads to a force constant that cannot be defined through Fourier transform as in the long wavelength limit, the force constant diverges. Such divergence can be resolved by adding a correction term — the nonanalytic force constant.

2.3.1 Nonanalytical force constant in polar materials

The Born effective charge is a tensor defined by,

$$eZ_s^{*\alpha\beta} = \Omega \left. \frac{\partial P_\alpha}{\partial u_s^\beta(\mathbf{q}=0)} \right|_{\mathbf{E}=0}, \quad (2.30)$$

where P_α is the polarization vector due to atom displacements. In first-principle calculation, the polarization per unit cell is written as,

$$P_\alpha = \frac{1}{\Omega} \sum_{s,\beta} eZ_s^{*\alpha\beta} u_{s,\beta} + \frac{\epsilon_\infty^{\alpha\beta} - \delta_{\alpha\beta}}{4\pi} E_\beta. \quad (2.31)$$

Another important quantity that is related to the polarization is the high-frequency electronic dielectric constant tensor,

$$\epsilon_{\infty}^{\alpha\beta} = \delta_{\alpha\beta} + 4\pi \frac{\partial P_{\alpha}}{\partial E_{\beta}} \Big|_{\mathbf{u}_s(\mathbf{q}=0)=0}, \quad (2.32)$$

where $\delta_{\alpha\beta}$ is Kronecker delta. With the Born effective charge and dielectric constant being defined, the nonanalytic force constant writes,

$${}^{na}\tilde{C}_{ss'}^{\alpha\beta}(\mathbf{q}) = \frac{4\pi}{\Omega} e^2 \frac{(\mathbf{q} \cdot \mathbf{Z}_s^*)_{\alpha} (\mathbf{q} \cdot \mathbf{Z}_{s'}^*)_{\beta}}{\mathbf{q} \cdot \epsilon_{\infty} \cdot \mathbf{q}}. \quad (2.33)$$

In cubic systems, the transverse phonon mode does not induce long-range electrical field yet the longitudinal phonon mode does. Thus, the phonon frequency of longitudinal optical phonon mode is usually higher than the transverse optical phonon mode. In cubic materials, the longitudinal phonon frequency is,

$$\omega_{LO} = \sqrt{\omega_{TO}^2 + \frac{4\pi e^2 Z^*{}^2}{\Omega \epsilon_{\infty} M}}. \quad (2.34)$$

The frequency difference between longitudinal optical phonon and transverse optical phonon near Γ point in the Brillouin zone is named as LO-TO splitting. The nonanalytical force constant makes sure the correct LO-TO splitting in phonon dispersion.

2.3.2 The screening effect of free carriers on phonons

In highly-doped semiconductors, the free carriers can respond to the polarization generated by the ion. Effectively, the long-range electrical field that leads to LO-TO splitting is screened, shown in Fig. 2-1. To include the screening effect in our calculation, we will derive the correction term for the nonanalytical force constant. The *Lindhard dielectric function*, as derived in Appendix A, is,

$$\epsilon(q) = 1 + \frac{1}{2} \frac{k_{TF}^2}{q^2} + \frac{1}{2} \frac{k_{TF}^2 k_F}{q^2} \left(1 - \frac{q^2}{4k_F^2}\right) \ln \left| \frac{2k_F + q}{2k_F - q} \right| \quad (2.35)$$

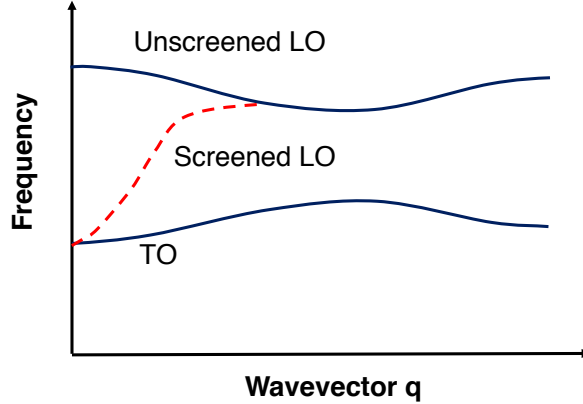


Figure 2-1: The screening effect of free carriers on the optical phonon modes. At the limit of $q \rightarrow 0$, the LO and TO modes converges given strong enough screening effect

where the Thomas-Fermi wavevector is defined by,

$$k_{TF}^2 = \frac{e^2}{\epsilon_0 \epsilon_\infty} \frac{\partial n}{\partial E_F} = -\frac{e^2}{\epsilon_0 \epsilon_\infty} \int g(\varepsilon) \frac{\partial f}{\partial \varepsilon} d\varepsilon. \quad (2.36)$$

In the parabolic band model, the Thomas-Fermi wavevector can be expressed as $k_{TF} = \sqrt{\frac{e^2 n}{\epsilon_0 \epsilon_\infty k_B T}}$. From Fig. 2-2, we find that the using the density of states from DFT calculation renders similar screening radius. The discrepancy is attributed to the non-parabolic nature of the band structures of PbTe. The k_F in Eq. 2.35 is the Fermi velocity. Equivalently,

$$\epsilon_L(q) = 1 + \frac{k_{TF}^2}{q^2} \left[\frac{1}{2} + \frac{1-x^2}{4x} \ln \left| \frac{1+x}{1-x} \right| \right] \quad (2.37)$$

where $x = q/2k_F$. Till now, the band is assumed to be parabolic, the Fermi energy should be much larger than $k_B T$. In fact, we find in PbTe that only small $|\mathbf{q}|$ can lead to strong Fröhlich interaction thus the choice of dielectric constant at large $|\mathbf{q}|$ would not affect the accuracy of the transport calculation. Furthermore, we argue that for those LO phonons that induce POP scattering, the phonon wavevector satisfies $|\mathbf{q}| \ll 2k_F$ in highly-doped PbTe. In such conditions, the Lindhard dielectric can be

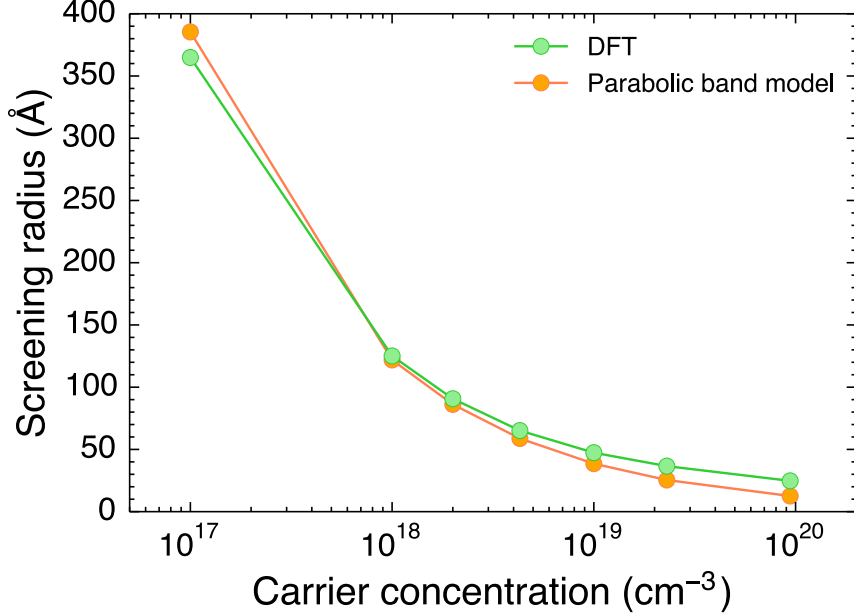


Figure 2-2: The inverse of the Thomas-Fermi wavevector ($1/k_{TF}$) — screening radius as a function of carrier density from DFT and from parabolic band model.

further reduced to Thomas-Fermi screening model,

$$\epsilon(q) = \epsilon_\infty \left(1 + \frac{k_{TF}^2}{q^2} \right), \quad (2.38)$$

where ϵ_∞ is ion-clamped (high frequency) macroscopic dielectric constant from DFPT[23][53].

After plugging in the dielectric constant in Eq.2.38 into Eq. 2.33, we can express the screened long-range force constant as,

$${}^{\text{na}}\tilde{C}_{ss'}^{\alpha\beta}(\mathbf{q}) = \frac{4\pi}{\Omega} e^2 \frac{(\mathbf{q} \cdot \mathbf{Z}_s^*)_\alpha (\mathbf{q} \cdot \mathbf{Z}_{s'}^*)_\beta}{|\mathbf{q}|^2 \epsilon_\infty \left(1 + \frac{k_{TF}^2}{q^2} \right)}. \quad (2.39)$$

2.3.3 Phonon dispersion of PbTe with different carrier concentrations

The force constant in Eq. 2.28 is defined on a uniform q-point mesh in standard DFPT calculation. To capture the long-range feature of LO phonon, we directly subtract the force constant with nonanalytical force constant described by Eq. 2.33 to obtain

a purely short-range force constant. Then, we add back the screened long-range force constant in Eq. 2.39 to examine the case the excess free carriers due to doping. In the calculation, we use a $6 \times 6 \times 6$ q -point mesh. In order to match the bulk phonon dispersion with neutron scattering, a Born effective charge of $Z^* = 5.8$ and a dielectric constant of 32 from Ref.[36] are adopted.

We demonstrate the consequence of the screening effect: the weakened LO-TO splitting, by calculating the phonon dispersion with various carrier concentrations. In Fig. 3-4 (c), we clearly observe that as the carrier concentration increases, the gap between LO and TO phonons near zone center is progressively narrowed. In the high-carrier-concentration limit and the long-wavelength limit, one should no longer be able to distinguish a LO and TO phonon since the screening length has becomes so small that the long-range dipole field responsible for the LO-TO splitting vanishes. The convergence of long-wavelength LO and TO phonon reminds us to examine whether it gives rise to stronger anharmonicity since TO phonon contributes remarkably to phonon-phonon scattering in PbTe[12]. However, we do not observe any noticeable difference after carrying out thermal conductivity calculation, because an only small fraction of LO phonons become TO phonons such that the three-phonon scattering phase space is barely modified.

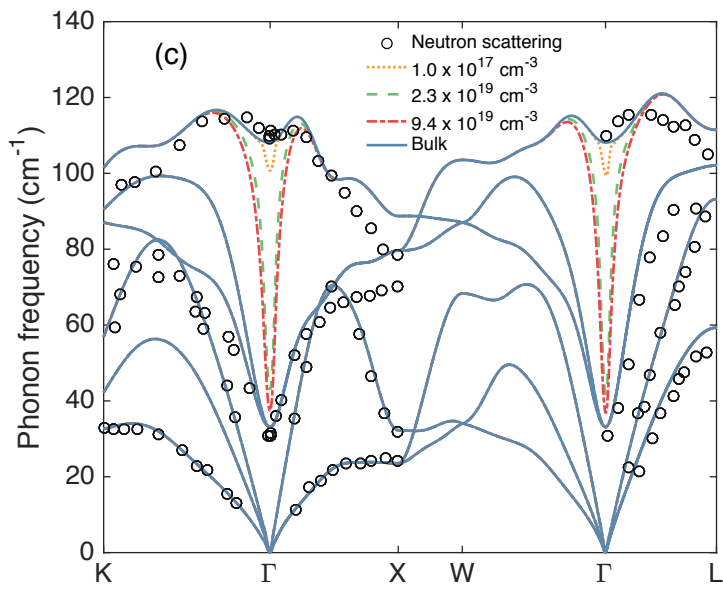


Figure 2-3: The phonon dispersion for different free carrier concentrations compared with neutron scattering experiment[10].

Chapter 3

Electron-phonon interaction in from first principles

The electron-phonon interaction is a fundamental type of interaction in solids that significantly influences the transport of electrons. The superconductivity, Joule heating, thermal relaxation of electrons, Raman spectroscopy *et al.* are all closely related to electron-phonon interaction. Despite a very long history of study of electron-phonon interaction, an accurate, fully first-principle formalism was not accessible until recently, as the dimensions of the quantity of interest is huge. Thus, the *ab initio* electron-phonon coupling calculation can be computationally infeasible. In this Chapter, we will introduce a scheme named electron-phonon Wannier interpolation which allows us to calculate electron-phonon interaction with relatively low cost and high accuracy.

3.1 Electron-phonon interaction to the lowest order

The Hamiltonian of a coupled electron-phonon system is[20]:

$$\begin{aligned} \hat{H} = & \sum_{n\mathbf{k}} \varepsilon_{n\mathbf{k}} \hat{c}_{n\mathbf{k}}^\dagger \hat{c}_{n\mathbf{k}} + \sum_{\mathbf{q}\nu} \hbar\omega_{\mathbf{q}\nu} (\hat{a}_{\mathbf{q}\nu}^\dagger \hat{a}_{\mathbf{q}\nu} + 1/2) \\ & + N_p^{-1/2} \sum_{\substack{\mathbf{k}, \mathbf{q} \\ mn\nu}} g_{mn\nu}(\mathbf{k}, \mathbf{q}) \hat{c}_{m\mathbf{k}+\mathbf{q}}^\dagger \hat{c}_{n\mathbf{k}} (\hat{a}_{\mathbf{q}\nu} + \hat{a}_{-\mathbf{q}\nu}^\dagger) \\ & + \left[N_p^{-1} \sum_{\substack{\mathbf{k}, \mathbf{q}, \mathbf{q}' \\ mn\nu\nu'}} g_{mn\nu\nu'}^{\text{DW}}(\mathbf{k}, \mathbf{q}, \mathbf{q}') \hat{c}_{m\mathbf{k}+\mathbf{q}+\mathbf{q}'}^\dagger \hat{c}_{n\mathbf{k}} (\hat{a}_{\mathbf{q}\nu} + \hat{a}_{-\mathbf{q}\nu}^\dagger) (\hat{a}_{\mathbf{q}'\nu'} + \hat{a}_{-\mathbf{q}'\nu'}^\dagger) \right], \end{aligned} \quad (3.1)$$

where $\varepsilon_{n\mathbf{k}}$ is the eigen-energy of an electron state with wavevector \mathbf{k} in the branch n , while $\omega_{\mathbf{q}\nu}$ is the frequency of a phonon state with wavevector \mathbf{q} in the branch ν . The creation operator $\hat{c}_{n\mathbf{k}}^\dagger$ creates an electron state $|n\mathbf{k}\rangle$ and the annihilation operator annihilates an electron state $|n\mathbf{k}\rangle$. Similarly, the creation operator $\hat{a}_{\mathbf{q}\nu}^\dagger$ creates a phonon state $|\mathbf{q}\nu\rangle$ and the annihilation operator $\hat{a}_{\mathbf{q}\nu}^\dagger$ annihilates a phonon state $|\mathbf{q}\nu\rangle$. N_p is the number of unit cells in a periodic supercell. In the first line of the equation, electrons and phonons are described separately. The second line of the equation corresponds to the electron-phonon coupling to the first order of the atom's lifetime displacements[44]. The third line of the equation describes the higher-order electron-phonon interaction.

The electron-phonon coupling matrix to the lowest-order approximation is given by,

$$g_{mn}^\nu(\mathbf{k}, \mathbf{q}) = \left(\frac{\hbar}{2m_0\omega_{\nu\mathbf{q}}} \right)^{\frac{1}{2}} \left\langle \psi_{m\mathbf{k}+\mathbf{q}} \left| \frac{\partial V_{\text{SCF}}}{\partial \mathbf{u}_{\nu\mathbf{q}}} \cdot \mathbf{e}_{\nu\mathbf{q}} \right| \psi_{n\mathbf{k}} \right\rangle, \quad (3.2)$$

where m_0 is the electron rest mass, $\psi_{n\mathbf{k}}$ is the electron wavefunction. The lowest-order electron-phonon interaction is responsible for the broadening of the electron states (i.e. the finite lifetime of electrons). $\partial V_{\text{SCF}} / \partial \mathbf{u}_{\nu\mathbf{q}} \cdot \mathbf{e}_{\nu\mathbf{q}}$ is the first-order variation of the self-consistent potential energy due to the presence of a phonon, as depicted Eq. 2.22 in Chapter 2.

The higher-order Debye-Waller term of electron-phonon coupling matrix is given

by,

$$g_{mn\nu\nu'}^{\text{DW}}(\mathbf{k}, \mathbf{q}, \mathbf{q}') = \frac{\hbar}{2m_0\omega_{\nu\mathbf{q}}\omega_{\nu'\mathbf{q}'}} \left\langle \psi_{m\mathbf{k}+\mathbf{q}+\mathbf{q}'} \left| \frac{\partial V_{\text{SCF}}}{\partial \mathbf{u}_{\nu\mathbf{q}}} \cdot \mathbf{e}_{\nu\mathbf{q}} \frac{\partial V_{\text{SCF}}}{\partial \mathbf{u}_{\nu'\mathbf{q}'}} \cdot \mathbf{e}_{\nu'\mathbf{q}'} \right| \psi_{n\mathbf{k}} \right\rangle. \quad (3.3)$$

It is believed that Debye-Waller term is responsible for the band energy renormalization: at high temperatures, the electronic bands can be significantly modified by the electron-phonon interaction. In narrow-band-gap thermoelectric materials like PbTe, the band gap is strongly dependent on temperature due to Debye-Waller type of electron-phonon scattering[63]. The higher-order coupling is complicated to be computed and beyond the scope of this thesis.

3.2 Electron-phonon Wannier interpolation

The energy of electrons is around several eV, while the energy of phonons is in meV scale. The phonon absorption where $n\mathbf{k} + \nu\mathbf{q} \rightarrow m\mathbf{k}'$ requires that the momentum is conserved with discrete translational symmetry: $\mathbf{k} + \mathbf{q} = \mathbf{k}' + \mathbf{G}$ (\mathbf{G} is the reciprocal lattice vector). More importantly, the energy conservation requires $\varepsilon_{n\mathbf{k}} + \hbar\omega_{\nu\mathbf{q}} = \varepsilon_{m\mathbf{k}'}$. Similarly, the phonon emission process where $n\mathbf{k} \rightarrow \nu\mathbf{q} + m\mathbf{k}'$ requires that $\mathbf{k} = \mathbf{q} + \mathbf{k}' + \mathbf{G}$ and $\varepsilon_{n\mathbf{k}} = \hbar\omega_{\nu\mathbf{q}} + \varepsilon_{m\mathbf{k}'}$. Due to the large mismatch in energy between electrons and phonons, a very dense k -point mesh is needed for direct calculation in the search of possible electron-phonon scattering modes such that energy and momentum conservation can be satisfied. The resultant severe computational challenge demands alternative approaches to obtain the electron-phonon coupling matrix.

3.2.1 Maximumly localized Wannier function

In periodic solids, the translational symmetry leads to the *Bloch's theorem* where the Bloch orbitals are Bloch amplitude multiplied by the phase which extends to the whole material. The Bloch orbitals are eigenstates of Hamiltonian. The Wannier function, localized in real space, is transformed from Bloch orbital[47]. For Bloch function, each

orbital is marked with a \mathbf{k} and it has a well-defined energy. For Wannier function, however, we cannot find the energy level of the orbital as it is a band. Thus we say we the localization in real space of Wannier function is achieved by losing localization in energy.

The Wannier function is defined by unitary transform (preserving the length of a vector),

$$|m\mathbf{R}_e\rangle = \sum_{n\mathbf{k}} e^{-i\mathbf{k}\cdot\mathbf{R}} U_{nm,\mathbf{k}} |n\mathbf{k}\rangle, \quad (3.4)$$

where $U_{nm,\mathbf{k}}$ is a unitary matrix. The plane wave basis can be recovered through inverse Fourier transform,

$$|n\mathbf{k}\rangle = \frac{1}{N_e} \sum_{m\mathbf{R}} e^{-i\mathbf{k}\cdot\mathbf{R}} U_{nm,\mathbf{k}}^\dagger |m\mathbf{R}_e\rangle. \quad (3.5)$$

The idea of the Wannier function is to find an alternative basis to replace plane wave basis. Since the number of Wannier functions per unit cell is the number of electrons per unit cell, much smaller than the number of plane waves typically used in DFT calculation, the computational cost can potentially be reduced. Apparently, the unitary transformation is not unique, as long as the Wannier functions are orthogonal. A localization criterion is proposed by Marzari and Vanderbilt[47] to obtain the maximumly localized Wannier function iteratively. The localization functional is defined by,

$$\Omega = \sum_n \left[\langle n\mathbf{0}|r^2|n\mathbf{0}\rangle - \langle n\mathbf{0}|r|n\mathbf{0}\rangle^2 \right]. \quad (3.6)$$

This quantity is actually the quadratic spreads of Wannier function around their centers in the home unit cell. By minimizing the localization functional through refining the unitary matrix $U_{nm,\mathbf{k}}$, we are able to obtain the maximumly localized Wannier function. The Wannier function can be calculated using Wannier90[51] package once we have the Bloch orbitals from DFT calculation. In Fig. 3-1, the maximumly localized Wannier functions of Pb and Te atom in PbTe are shown. Different color of the isosurface (iso-charge-density) indicates the opposite sign of the values of Wannier orbitals. The shape of isosurface displays the character of σ -bounded combination of

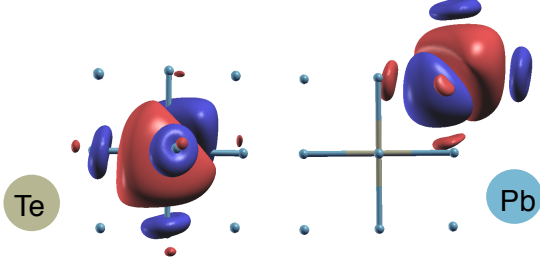


Figure 3-1: The maximumly localized Wannier orbitals of Pb and Te in PbTe without spin-orbit coupling. The symmetry of the material is not conserved during the iterative process of minimizing the localization functional.

p orbitals. However, the symmetry revealed by maximum localized Wannier function is lower than the crystal symmetry. This is because of the lack of symmetry constraint in the localization functional in Eq. 3.6.

3.2.2 Electron-phonon coupling matrix in the Wannier representation

In order to proceed to construct the electron-phonon coupling matrix in Wannier representation, we need to first discuss the perturbation due to phonon in the Wannier representation,

$$\partial_{\mathbf{q}\nu} V(\mathbf{r}) = \sum_{\kappa, \mathbf{R}_p} e^{i\mathbf{q}\cdot\mathbf{R}_p} \mathbf{u}_{\kappa}^{\nu} \cdot \partial_{\kappa, \mathbf{R}_p} V(\mathbf{r}), \quad (3.7)$$

where the displacement $u_{\mathbf{q}\kappa}^{\nu} = (m_0/m_{\kappa})^{1/2} \mathbf{e}_{\mathbf{q}\kappa}^{\nu}$. The inverse transform from Bloch representation to Wannier representation reads,

$$\partial_{\kappa, \mathbf{R}_p} V(\mathbf{r}) = \frac{1}{N_p} \sum_{\mathbf{q}\nu} e^{-i\mathbf{q}\cdot\mathbf{R}_p} [u_{\mathbf{q}\kappa}^{\nu}]^{-1} \partial_{\mathbf{q}\nu} V(\mathbf{r}). \quad (3.8)$$

Then, we can rewrite the electron-phonon coupling matrix defined in Eq. 3.2 in the Wannier representation:

$$\begin{aligned} \left\langle m\mathbf{k} + \mathbf{q} \left| \frac{\partial V_{\text{SCF}}}{\partial \mathbf{u}_{\nu\mathbf{q}}} \cdot \mathbf{e}_{\nu\mathbf{q}} \right| n\mathbf{k} \right\rangle &= \frac{1}{N_e^2} \sum_{m'n'\kappa} \sum_{\mathbf{R}_e \mathbf{R}'_e \mathbf{R}_p} e^{i[\mathbf{k}\cdot(\mathbf{R}_e - \mathbf{R}'_e) + \mathbf{q}\cdot(\mathbf{R}_p - \mathbf{R}'_e)]} \\ &\times \mathbf{u}_{\mathbf{q}\kappa}^{\nu} \cdot U_{mm',\mathbf{k}+\mathbf{q}} \left\langle m' \mathbf{R}_e \left| \partial_{\kappa, \mathbf{R}_p} V_{\text{SCF}} \right| n' \mathbf{R}_e \right\rangle U_{n'n\mathbf{k}}^{\dagger}. \end{aligned} \quad (3.9)$$

Using the translational symmetry of the matrix, we can simplify the matrix element in Wannier representation as,

$$g(\mathbf{k}, \mathbf{q}) = \frac{1}{N_e} \sum_{\mathbf{R}_e, \mathbf{R}_p} e^{i(\mathbf{k} \cdot \mathbf{R}_e + \mathbf{q} \cdot \mathbf{R}_p)} U_{\mathbf{k}+\mathbf{q}} g(\mathbf{R}_e, \mathbf{R}_p) U_{\mathbf{k}}^\dagger \mathbf{u}_q, \quad (3.10)$$

where electron-phonon matrix in Wannier representation is,

$$\begin{aligned} g_{mn,\nu}(\mathbf{R}_e, \mathbf{R}_p) &= \langle m \mathbf{0}_e | \partial_{\nu, \mathbf{R}_p} V | n \mathbf{R}_e \rangle \\ &= \frac{1}{N_p} \sum_{\mathbf{k}, \mathbf{q}} e^{-i(\mathbf{k} \cdot \mathbf{R}_e + \mathbf{q} \cdot \mathbf{R}_p)} U_{\mathbf{k}+\mathbf{q}}^\dagger g(\mathbf{k}, \mathbf{q}) U_{\mathbf{k}} \mathbf{u}_{\mathbf{q}}^{-1} \end{aligned} \quad (3.11)$$

where the last term the band index n and m is hidden. It is shown by [21] that the matrix element $g_{mn,\nu}(\mathbf{R}_e, \mathbf{R}_p)$ vanishes at the distance of several unit cells to the origin, the localized feature of the matrix element allows us to interpolate the matrix over a dense mesh without costing too much computational resource.

3.3 Electron-phonon coupling matrix in polar materials

3.3.1 Screened Fröhlich interaction

In polar materials, the standard Wannier interpolation fail to reproduce the correct electron-phonon coupling matrix elements in the small q limit. This is because: similar to the origin of LO-TO slitting where long-range dipole field emerges due to longitudinal optical phonon, the same field induces interaction between electrons and optical phonons, known as Fröhlich interaction. The electron-phonon coupling matrix can be decomposed into two parts,

$$g_{n\mathbf{k}, \nu\mathbf{q}}^{m\mathbf{k}+\mathbf{q}} = g_{n\mathbf{k}, \nu\mathbf{q}}^{m\mathbf{k}+\mathbf{q}, \text{short}} + g_{n\mathbf{k}, \nu\mathbf{q}}^{m\mathbf{k}+\mathbf{q}, \text{long}}. \quad (3.12)$$

The form of the long-range electron-phonon coupling matrix writes,

$$g_{n\mathbf{k},\nu\mathbf{q}}^{m\mathbf{k}+\mathbf{q}, \text{long}} = \frac{ie^2}{\Omega\epsilon_0} \sum_{s,\mathbf{G}\neq-\mathbf{q}} \left(\frac{\hbar}{2NM_s\omega_{\nu\mathbf{q}}} \right)^{1/2} \times \frac{(\mathbf{q} + \mathbf{G}) \cdot \mathbf{Z}_s^* \cdot \mathbf{e}_{sp}(\mathbf{q})}{(\mathbf{q} + \mathbf{G}) \cdot \boldsymbol{\epsilon}_\infty \cdot (\mathbf{q} + \mathbf{G})} \langle m\mathbf{k} + \mathbf{q} | e^{i(\mathbf{q} + \mathbf{G}) \cdot \mathbf{r}} | n\mathbf{k} \rangle, \quad (3.13)$$

where \mathbf{G} is the lattice site in the reciprocal space. Apparently, the long-range electron-phonon coupling is $|g_{n\mathbf{k},\nu\mathbf{q}}^{m\mathbf{k}+\mathbf{q}, \text{long}}| \sim 1/|\mathbf{q} + \mathbf{G}|$, leading to divergence in Fourier transform.

The presence of free carriers can modulates the strength of the long-range electron-phonon coupling by screening the dipole field of LO phonon. Similar to the procedures to include screening effect in Sec. 2.3.3, we can express the screened long-range electron-phonon matrix element viz.,

$$g_{n\mathbf{k},\nu\mathbf{q}}^{m\mathbf{k}+\mathbf{q}, \text{long}} = \frac{ie^2}{\Omega\epsilon_0} \sum_{s,\mathbf{G}\neq-\mathbf{q}} \left(\frac{\hbar}{2NM_s\omega_{\nu\mathbf{q}}} \right)^{1/2} \times \frac{(\mathbf{q} + \mathbf{G}) \cdot \mathbf{Z}_s^* \cdot \mathbf{e}_{sp}(\mathbf{q})}{|\mathbf{q} + \mathbf{G}|^2 \cdot \boldsymbol{\epsilon}_\infty \cdot \left(1 + \frac{k_{TF}^2}{q^2} \right)} \langle m\mathbf{k} + \mathbf{q} | e^{i(\mathbf{q} + \mathbf{G}) \cdot \mathbf{r}} | n\mathbf{k} \rangle. \quad (3.14)$$

When the Thomas-Fermi wavevector is small, the nonanalytical feature still remains. Note that the DFPT calculation is defined on a grid, e.g. $6 \times 6 \times 6$. This is equivalent to a real-space calculation for a $6 \times 6 \times 6$ supercell. In principle, one can successively increases size of the mesh used in DFPT calculation to capture the long-range feature of the LO phonon. In practice, the largest size of the supercell that is computationally achievable is still much smaller compared with typical characteristic length of dipole field generated by LO phonon. To deal with such dilemma, we will first subtract the long-range part of electron-phonon coupling matrix in the Bloch representation with the form in Eq. 3.13. The resultant part of the electron-phonon coupling matrix is short-range. The short-range feature guarantees fidelity of Wannier transformation. We then construct the electron-phonon matrix element in the Wanner representation based on such short-range matrix element. Starting with the localized Wannier matrix element, we apply an inverse transform to obtain the short-range electron-phonon

matrix element on a very fine-mesh (in this calculation, $200 \times 200 \times 200$ implemented in a home-modified version of the EPW code[57]). Finally, we add back the screened long-range electron-phonon matrix in Eq.3.14 on the same fine mesh and obtain the full electron-phonon coupling matrix on a very fine mesh. Note that when we do the subtraction, we have not included the screening effect as the perturbation by phonon from DFPT calculation is calculated in a pristine bulk system without any excess carrier, which requires us to use the non-screened form of the long-range electron-phonon coupling element in the subtraction.

3.3.2 Electron-phonon coupling matrix for different phonon polarization in PbTe

Electrons at L point. The conduction band minimum of PbTe is at L point. To understand the coupling between the electrons at band edge and phonons, the electron-phonon coupling matrix including the screened/unscreened Fröhlich part and short-range part is calculated, shown in Fig. 3-2. For all acoustic phonons and transverse optical phonons, the screening effect does not lead to any difference. For LO phonon with large q , the screening effect is negligible as the alignment of ions with opposite charges is short-range, creating very weak dipole field. For LO phonon with small q near the Γ point, the screening effect slightly reduces the strength of electron-LO-phonon coupling. Particularly, the screening effect does not remove the divergence near the Γ point ($|g| \sim q^{-1}$). In addition, the electron-phonon coupling strength for LO phonons only dominates over other phonon branches when q is small. For example, for phonons with q on the path $X \rightarrow \Gamma$, the coupling between electron and TO phonon is strong except near the Γ point. For phonons at L point, the coupling between electron and LO phonon is strongest among all phonon branches. However, such strong coupling does not contribute to the scattering rate since energy conservation is not satisfied: $\hbar\omega_{\text{LO,L}} < \varepsilon_\Gamma - \varepsilon_L$.

Electrons away from L point. Since the electron at L point has zero group velocity, we want to understand the coupling between phonons and electrons away from L

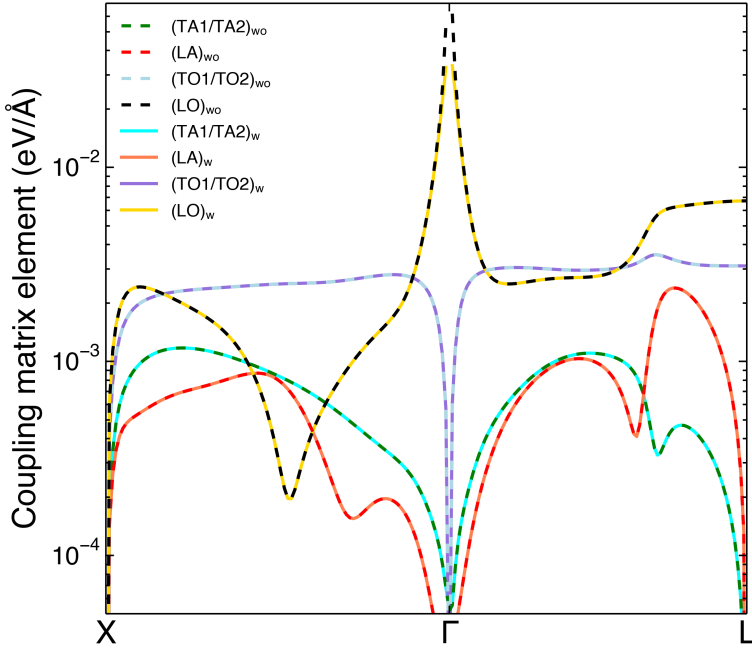


Figure 3-2: The amplitude of the electron-phonon coupling matrix element for electron at conduction band minimum and phonons at the high-symmetry paths with/without considering screening in the long-range (Fröhlich) part of the electron-phonon coupling matrix. The carrier concentration is 10^{18}cm^{-3} .

point with finite group velocity as well. In Fig. 3-3 (a), we present the coupling strength between electrons at high-symmetry path and LO phonons at high-symmetry path. As the phonon wavevector approaches the zone boundary, the electron-phonon coupling strength decreases with electron moving away from the bottom of L valley. As the phonon wavevector approaches Γ point, the coupling strength is largest when the electron is around $L + 0.3 \times (\Gamma - L)$. Overall, the electron-phonon coupling strength decreases as phonon wavevector increases. In the low q limit, the electron-phonon coupling is independent of the wavevector of electrons, as shown in Fig. 3-3 (b).

The coupling between TO phonon and electrons is demonstrated in Fig. 3-3 (c). We find that the coupling between TO phonons and electron at the L valley bottom is strongest among all phonon polarizations except that for $q \rightarrow 0$ the electron-phonon strength rapidly approaches 0. Also, aside from $q \rightarrow 0$, the coupling strength decreases

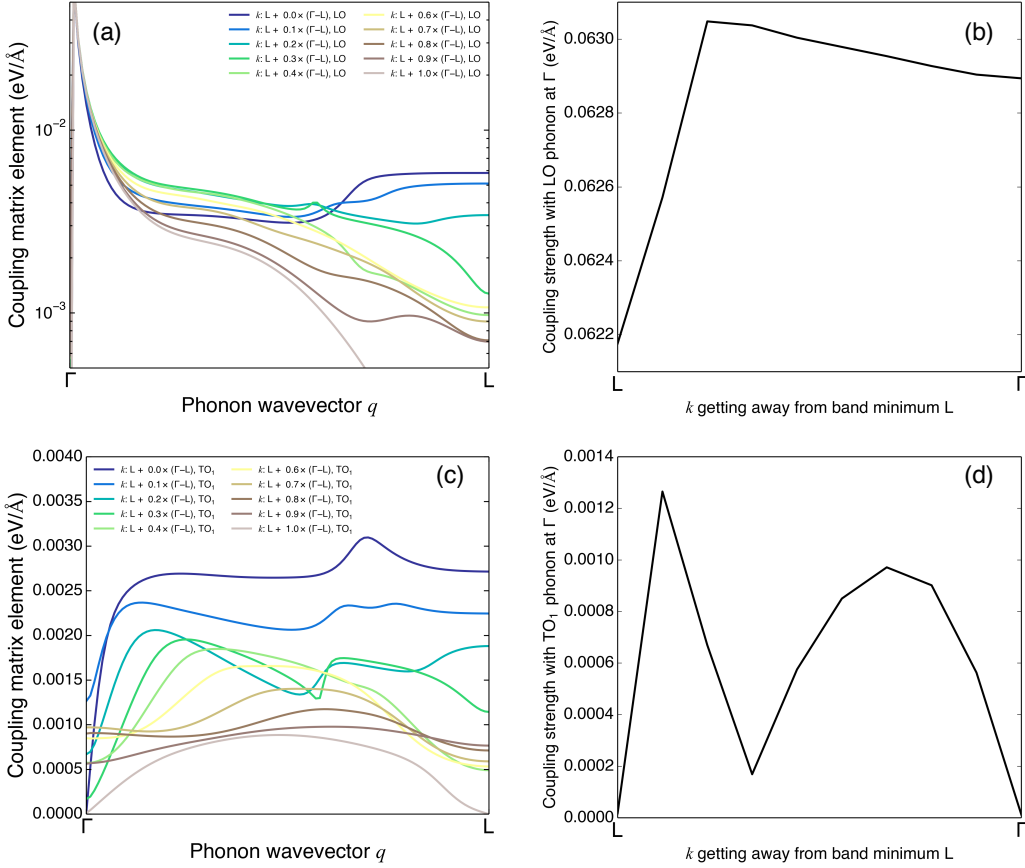


Figure 3-3: The amplitude of the electron-phonon coupling matrix element including screening effect for electrons at $L \rightarrow \Gamma$ path and LO/TO phonons at $\Gamma \rightarrow L$. In (a) and (c), different colors mark different electron states. In (b) and (d), the strength of the coupling between Γ point LO/TO phonon and different electron states are shown. Note that for LO phonon, the exact $q = 0$ behavior cannot be calculated due to the divergence shown in Eq. 3.14 thus we use $q = 0.01 \times l_{\Gamma L} = 0.01 \times \frac{\sqrt{3}\pi}{2a}$ to represent the extreme case $q = 0$. The carrier concentration is 10^{18} cm^{-3} .

when the electron gets away from the bottom of the L valley. As shown in Fig. 3-3 (d), we find that near the L point, the coupling strength is exactly 0 while it rapidly increases with the electron moving away from valley bottom. Similarly, the coupling strength starts from 0 and increases as electron is further away from Γ point towards L point. For the phonon near the middle of L and Γ point, there is a local minimum of the electron-phonon coupling matrix. At this stage, we cannot explain clearly the origin of the complicated trend of the electron-phonon coupling as a function of k and q . However, we can expand the band structure using $\mathbf{k} \cdot \mathbf{p}$ method near the band extreme and express the electron-phonon coupling matrix in the low k and low q limit.

Meanwhile, we need to take into account the crystal symmetry of PbTe to unveil the root of zero electron-phonon coupling strength at certain high-symmetry point.

3.4 Relaxation time approximation

3.4.1 Electron-phonon scattering rate

The electron-phonon self-energy based on Migdal approximation[48] is defined by,

$$\Sigma_{n\mathbf{k}} = \sum_{m\nu q} |g_{mn}^\nu(\mathbf{k}, \mathbf{q})|^2 \left[\frac{n_{\nu\mathbf{q}} + f_{m\mathbf{k}+\mathbf{q}}}{\epsilon_{n\mathbf{k}} - \epsilon_{m\mathbf{k}+\mathbf{q}} + \hbar\omega_{\nu\mathbf{q}} - i\eta} + \frac{n_{\nu\mathbf{q}} + 1 - f_{m\mathbf{k}+\mathbf{q}}}{\epsilon_{n\mathbf{k}} - \epsilon_{m\mathbf{k}+\mathbf{q}} - \hbar\omega_{\nu\mathbf{q}} - i\eta} \right], \quad (3.15)$$

where $g_{mn}^\nu(\mathbf{k}, \mathbf{q})$ is the electron-phonon coupling matrix element in Bloch representation and $n_{\nu\mathbf{q}}$ is the phonon distribution. $\epsilon_{n\mathbf{k}}$ is the electron energy and $\omega_{\nu\mathbf{q}}$ is the phonon frequency.

The electron-phonon scattering rate can be calculated from the imaginary part of self-energy $\Sigma_{n\mathbf{k}}$ by $\Gamma_{n\mathbf{k}} = 1/\hbar \text{Im } \Sigma_{n\mathbf{k}}$. The explicit form of the electron-phonon scattering rate can be written as,

$$\begin{aligned} \Gamma_{n\mathbf{k}} &= \sum_{m\nu q} \frac{\pi}{\hbar} |g_{mn}^\nu(\mathbf{k}, \mathbf{q})|^2 \\ &\times \left[(n_{\nu\mathbf{q}} + 1 - f_{m\mathbf{k}+\mathbf{q}}) \delta(\epsilon_{n\mathbf{k}} - \epsilon_{m\mathbf{k}+\mathbf{q}} - \hbar\omega_{\nu\mathbf{q}}) \right. \\ &\quad \left. + (n_{\nu\mathbf{q}} + f_{m\mathbf{k}+\mathbf{q}}) \delta(\epsilon_{n\mathbf{k}} - \epsilon_{m\mathbf{k}+\mathbf{q}} + \hbar\omega_{\nu\mathbf{q}}) \right]. \end{aligned} \quad (3.16)$$

The inverse of the scattering rate gives the relaxation time, $\tau_{n\mathbf{k}} = 1/\Gamma_{n\mathbf{k}}$.

$$\begin{aligned} \frac{1}{\tau_{n\mathbf{k}}} &= \frac{2\pi}{\hbar} \sum_{m,\nu\mathbf{q}} \left| g_{n\mathbf{k},\nu\mathbf{q}}^{m\mathbf{k}+\mathbf{q}} \right|^2 \times \left[(n_{\nu\mathbf{q}} + 1 - f_{m\mathbf{k}+\mathbf{q}}) \delta(\epsilon_{n\mathbf{k}} - \epsilon_{m\mathbf{k}+\mathbf{q}} - \hbar\omega_{p\mathbf{q}}) \right. \\ &\quad \left. + (n_{p\mathbf{q}} + f_{m\mathbf{k}+\mathbf{q}}) \delta(\epsilon_{n\mathbf{k}} - \epsilon_{m\mathbf{k}+\mathbf{q}} + \hbar\omega_{p\mathbf{q}}) \right]. \end{aligned} \quad (3.17)$$

The electron-phonon scattering rates due to different phonon branches without considering the screening effect is shown in Fig. 3-4 (a). The scattering due to LO

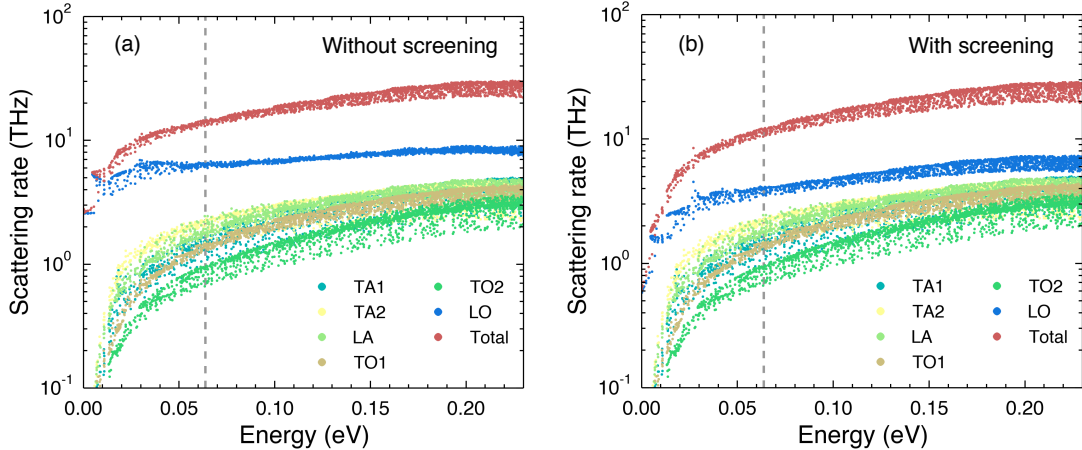


Figure 3-4: (a-b) The energy-resolved electron-phonon scattering rates for conduction band electrons due to phonon modes of different branches at 300 K with/without considering the screening effect. The zero energy marks the conduction band minimum and the dashed line indicates the location of chemical potential. The carrier concentration is $2.3 \times 10^{19} \text{ cm}^{-3}$.

phonons is stronger than other phonon branches. Near the conduction band minimum, only phonon absorption process is allowed to happen. When electron energy is larger than energy of a LO phonon, both phonon absorption and emission can happen. This leads to the sudden jump in the scattering rate near 0.01 eV. Note that the dielectric constant calculated from DFPT is 104, which is overestimated compared with experiment reported value 32[10]. As a result, the LO phonon frequency is 10 meV from the calculation, which is underestimated than the value of the value of 13 meV found through neutron scattering experiment[10]. One interesting feature of the scattering rate due to LO phonon is the relatively weak energy dependence. The scattering due to LO phonon consists of two contributions: the non-polar optical phonon deformation potential (ODP) scattering and POP scattering, as discussed in detail in Ref.[41]. The non-polar ODP scattering rate scales with \sqrt{E} (E is the electron energy measured from conduction band edge), and the POP scattering rate scales with $\sinh^{-1}(\sqrt{E})$ assuming a parabolic band. The actual non-parabolic band structure of PbTe might change the exact energy dependence of scattering rates. Still qualitatively, the POP scattering rate increases less rapidly with increasing electron energy than the non-polar ODP scattering rate.

When including the screening effect shown in Fig. 3-4 (b), the scattering rate due to LO phonon decreases especially for low-energy electrons ($E < 0.1$ eV). At the conduction band minimum, because of the screening effect, the scattering rate due to LO phonon decreases from 2.5 THz to 0.5 THz. On the contrary, the reduction is much less noticeable for high-energy electrons. The screening effect in principle should only be able to affect POP scattering rather than ODP scattering. For high-energy electrons ($E > 0.1$ eV), non-polar ODP scattering is much stronger than POP scattering so that the reduction in POP scattering becomes less discernible than low-energy electrons.

Iterative BTE solver beyond RTA. The relaxation time approximation is valid when the phonon energy is negligible compared with the energy of electron[8][62]. Typically, the high energy of LO phonon involved in the polar scattering process in polar material make RTA invalid. By defining an effective electron mean free displacement $\mathbf{F}_{n\mathbf{k}}$, the deviation of the distribution function is subject to the equation,

$$f_{n\mathbf{k}} - f_{n\mathbf{k}}^0 = \frac{f_{n\mathbf{k}}^0(1 - f_{n\mathbf{k}}^0)}{k_B T} e \mathbf{E} \cdot \mathbf{F}_{n\mathbf{k}}. \quad (3.18)$$

After some numerical operations, the mean free displacement is subject to the relation,

$$\mathbf{F}_{n\mathbf{k}} = \tau_{n\mathbf{k}}^{\text{RTA}} \left[\mathbf{v}_{n\mathbf{k}} + [\tau_{n\mathbf{k}}^{\text{RTA}}]^{-1} \mathbf{F}_{n\mathbf{k}} \right] \quad (3.19)$$

By iteratively solving Eq. 3.19, we can obtain the transport properties derived in Sec. 1.2.2 by replacing $\mathbf{v}_{n\mathbf{k}} \tau_{n\mathbf{k}}$ with $\mathbf{F}_{n\mathbf{k}}$.

3.4.2 Phonon scattering rate by electrons

It's found by Liao[39][38] that the phonon scattering due to electron-phonon interaction is stronger as carrier density increases. In silicon with carrier concentration as high as 10^{21} cm $^{-3}$ the thermal conductivity is reduced by 45 % due to electron-phonon

interaction. The phonon scattering rate by electrons is defined by,

$$\frac{1}{\tau_{\nu\mathbf{q}}} = \frac{2\pi}{\hbar} \sum_{mn} \int \frac{d\mathbf{k}}{\Omega_{BZ}} \left| g_{n\mathbf{k},\nu\mathbf{q}}^{m\mathbf{k}+\mathbf{q}} \right|^2 (f_{n\mathbf{k}} - f_{m\mathbf{k}+\mathbf{q}}) \delta(\varepsilon_{m\mathbf{k}+\mathbf{q}} - \varepsilon_{n\mathbf{k}} - \hbar\omega_{\nu\mathbf{q}}) \quad (3.20)$$

In Fig. 3-5, the scattering rates for phonons due to electron-phonon interaction is

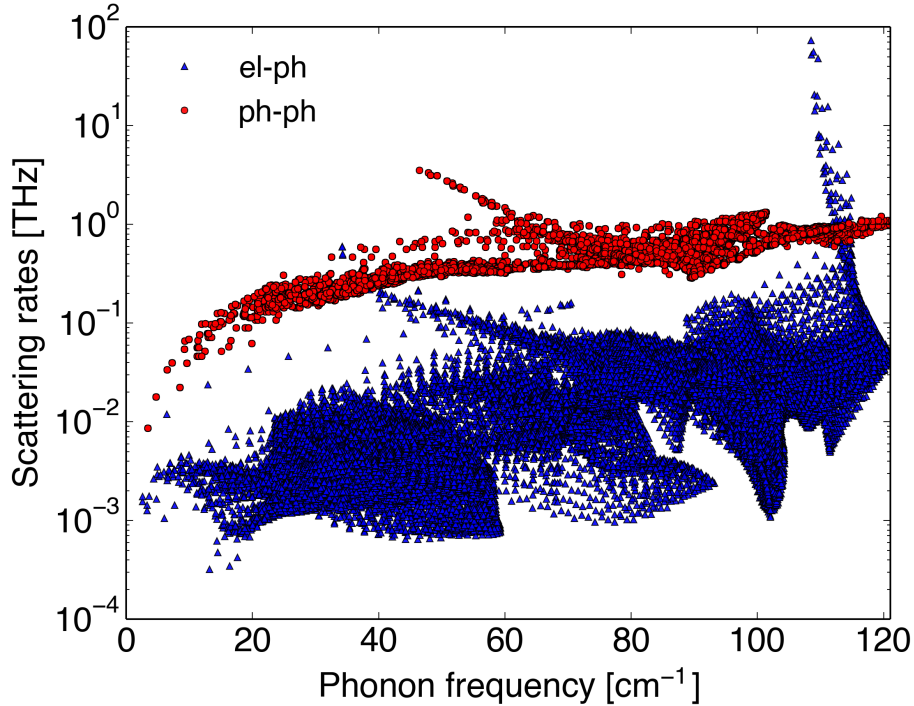


Figure 3-5: The scattering rate for phonons due to electron-phonon interaction compared with the scattering rate due to phonon-phonon interaction at 300 K with the carrier concentration of 10^{21}cm^{-3} .

plotted in comparison with the scattering rates due to phonon-phonon scattering. The phonon thermal conductivity is barely affected by the electron-phonon coupling, as the scattering rate due to electron-phonon interaction is negligible compared with phonon-phonon interaction. Nevertheless, there are still some interesting features especially compared with the scattering rate due to electron-phonon interaction in silicon. Firstly, there is no phonon bandgap in PbTe. As a result, the scattering rate due to electron-phonon interaction continuously increases as phonon frequency increases. In addition, the scattering rate due to electron-phonon interaction is highly sensitive to the momentum thus leading to a broad spread of the scattering rate at

given phonon frequency. Lastly, the scattering rate due to electron-phonon interaction exceeds the phonon-phonon scattering rate when phonon frequency is about 110 cm^{-1} . This energy is referred to the LO phonon at L point which can be scattered by low-energy electrons near conduction band minimum at L point into phonon states near the Γ point.

Chapter 4

The electron mean free paths and transport properties in PbTe

For PbTe, the thermal transport has also been examined from the first principles yielding that phonons with mean free paths smaller than 10 nm contribute the majority of the thermal conductivity[70]. However, its electron transport properties and electron mean free paths are much less understood. Past works have mostly employed the constant relaxation time approximation when studying the electrical transport properties of PbTe[64][75]. Although good agreements with experiments have been achieved for the Seebeck coefficient, the detailed information on the charge carrier dynamics remains unknown. In particular, by adopting the single/double Kane band model together with multiple scattering mechanisms, past works successfully explain the trend of the experimental findings[74][66][60][61], yet the analysis requires the fitting parameters extracted from experimental results thus not necessarily unveiling the correct physical pictures.

In this chapter, we evaluate the electron scattering rates and electron mean free paths due to electron-phonon interaction using first principles for *n*-type PbTe. By further comparing the mean free paths of electrons with phonons, we are able to thoroughly examine the electron transport and phonon transport in PbTe at the same time. The detailed spectral information on the thermoelectric properties of PbTe not only provides microscopic pictures of the dynamics of electron and phonon but can

be used to rationalize the design of the nanostructured PbTe to decouple electron and phonon transport in order to boost the thermoelectric performance. Finally, we try to understand the why PbTe has high mobility and high Seebeck coefficient in PbTe at the same time.

4.1 *Ab initio* thermoelectric transport properties

4.1.1 The effect of screening

The electron transport properties for *n*-type PbTe at room temperature with/without considering the screening effect of the free carriers are demonstrated in Fig. 4-1. The free carriers in doped PbTe screen the dipole field generated by ion vibration outside the sphere defined by the screening length. One thus expects reduced POP scattering and higher mobility after taking into account the screening effect. We notice from Fig. 4-1 that considering the screening effect does yield higher mobility and conductivity than without the screening effect, as well as a more desirable agreement with experiment even though the discrepancies in Seebeck coefficient and power factor for the two cases are not significant.

Fig. 4-2 (a) shows that the mean free path for low-energy electrons increases dramatically when including the screening effect. Although the LO phonon scattering is the prominent scattering source (both for cases with/without screening), it is not strong enough to totally overshadow the contribution from TO phonons and acoustic phonons. For electrons with energy near the chemical potential, the scattering of non-LO phonons contributes to the total scattering comparably with LO phonons. Note the electron group velocity near the chemical potential is weakly dependent on energy, as also shown in Ref.[9]. That is to say, the electron mean free path is a monotonically decreasing function of energy near the chemical potential because the electron relaxation time decreases monotonically with an increase in energy.

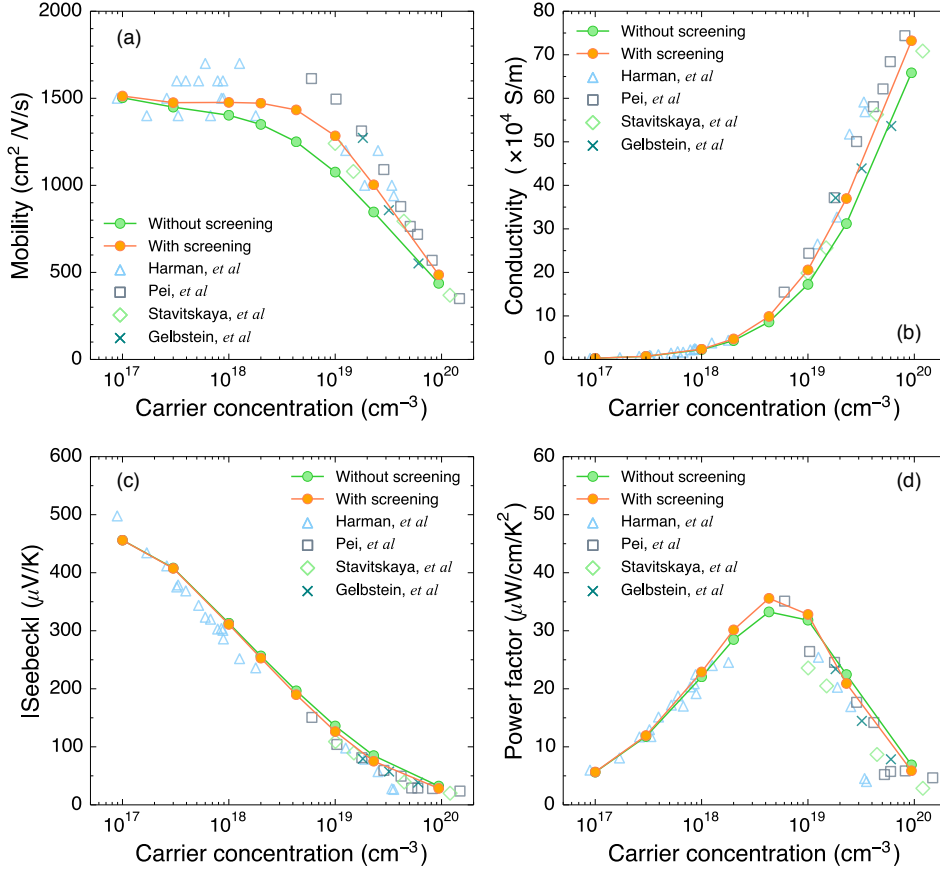


Figure 4-1: (a) The mobility, (b) the electrical conductivity, (c) the Seebeck coefficient, and (d) the power factor of PbTe as a function of carrier concentration at 300 K with and without considering the screening effect. Dotted lines are from simulation and isolated dots are experimental value. The triangles are from Ref.[26], squares from Ref.[54], diamonds from Ref.[67], and crosses from Ref.[15].

The electrical properties of electron as a function of electron mean free path is displayed in Fig. 4-2 (b), where the conductivity is enhanced by about 20 % due to the screening effect. Besides, the mean free path spectrum is shifted to higher values. An interesting feature is found in the truncated Seebeck coefficient in Fig. 4-2 (c): up to certain mean free path, the truncated Seebeck coefficient can be even higher than the total Seebeck coefficient. As is known, above the chemical potential, the electrons contribute dominantly to the Seebeck coefficient with negative signs. However, the electrons below the chemical potential have positive signs and they cancel the contribution of electrons above the chemical potential. Recall the mean

free path is almost a monotonically decreasing function of energy in Fig. 4-2 (a). The above observation then translates to the fact that the long-mean-free-path electrons contribute “negatively” to Seebeck whilst the short-mean-free-path ones contribute “positively”, which explains the emergence of the peak in the truncated Seebeck coefficient at a critical mean free path. The screening effect pushes the critical mean free path from 35 nm to 40 nm and the peak value rises from 160 % to 210 %. In Fig. 4-2 (d) the peak power factor at the critical mean free path is as high as 310 % with screening effect and 160 % without screening effect. We also find that the truncated power factor with/without screening effect at the long-mean-free-path limit are almost the same, albeit the screening effect greatly alters the mean free path distribution.

If we compare the truncated power factor to the cumulative thermal conductivity, we first realize that the major contribution to thermal conductivity is from phonons with mean free paths smaller than 20 nm, whilst for the truncated power factor, most contributions are from electrons with mean free paths higher than 20 nm. Surprisingly, this finding contradicts with the general case where the electron means free paths are much smaller than the phonon mean free paths, which emphasizes the importance of considering both electron and phonon when designing the nanostructures for PbTe. However, despite that nanostructures that scatter phonons may also scatter electrons, the long-mean-free-path electrons contributed negatively to the Seebeck coefficient. Nanostructures may scatter these long-mean-free-path electrons, leading to actually increased Seebeck coefficient and decreased electrical conductivity. This is seen in some of past experiments[69], although arguably, we cannot tell at this stage if these past experimental observations is due to filtering of long-mean-free-path electrons or the thermionic effect[73].

4.1.2 The effect of temperature

We proceed to study the temperature dependence of the transport properties. When raising the temperature, the mean free paths not only decreases but covers a narrower mean free path range, shown in Fig. 4-3. For electrons with the same energy, the

mean free path is not a single value but forming a “band” containing a series of possible values. The width of the “band” shrinks with rising temperature. At elevated temperatures, the population of phonons scales with T . From the analysis of our calculation, the scattering rate is directly related to temperature in a power law $\propto T$. Hence, for the electrons with the same energy, the scattering rates are rescaled by the temperature, and the inverse of the scattering — the relaxation time, will decrease and spread in a narrower region, causing a narrower “band”.

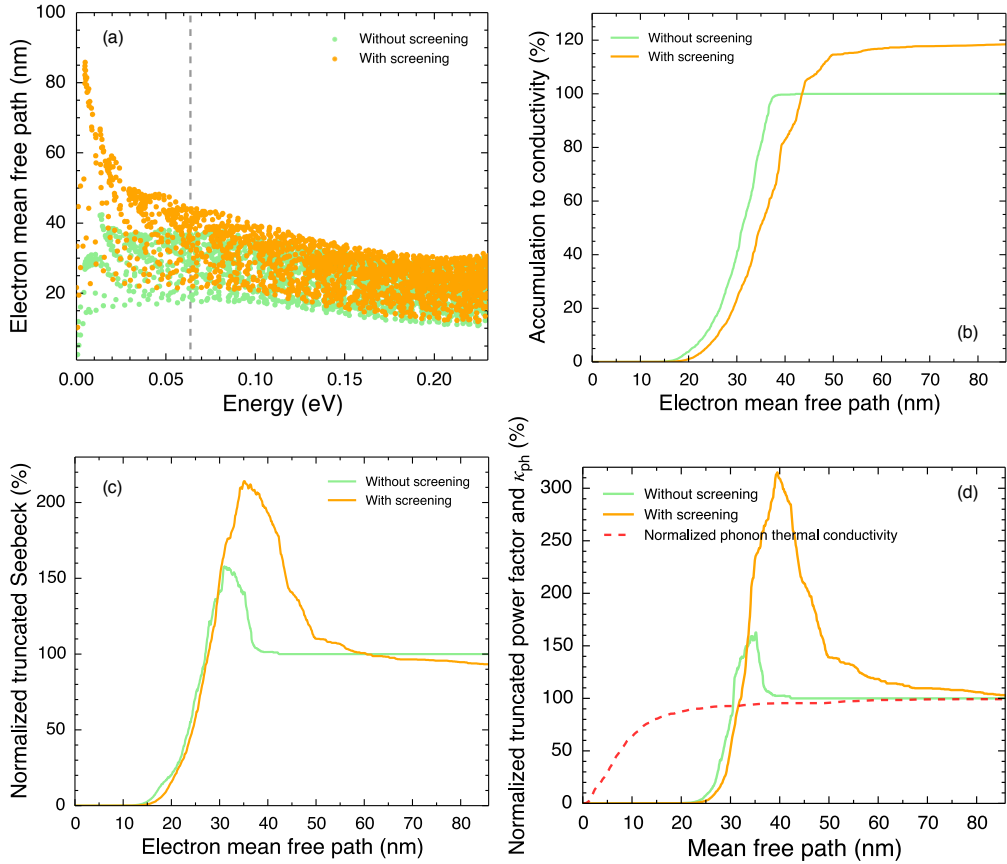


Figure 4-2: (a) The electron mean free path as a function of energy with and without considering the screening effect. The dashed line indicates the chemical potential and zero energy indicates the conduction band minimum. (b) The accumulated electrical conductivity with respect to electron mean free path. (c) The normalized truncated Seebeck coefficient with respect to the electron mean free path. (d) The normalized truncated power factor with respect to electron mean free path compared with normalized accumulated phonon thermal conductivity with respect to phonon mean free path. The dopant concentration is $2.3 \times 10^{19} \text{ cm}^{-3}$.

In addition, at higher temperatures, the chemical potential shifts towards the band

minimum. This is because the Fermi-Dirac distribution function spreads wider in the energy scale as temperature rises. To match the fixed amount of positively charged ionized donors, the chemical potential must be lowered.

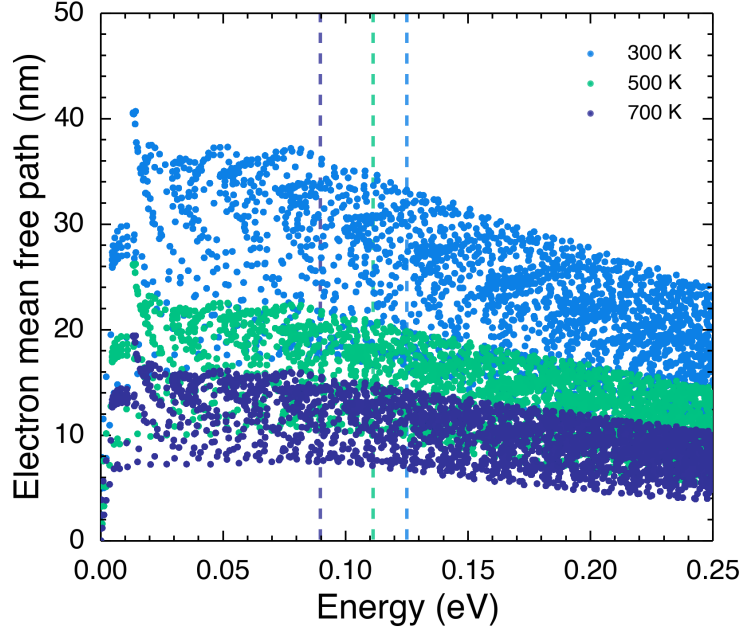


Figure 4-3: The electron mean free path as a function of energy at different temperatures. The dashed line indicates the chemical potential and zero energy corresponds the conduction band minimum. The dopant concentration is $5.8 \times 10^{19} \text{ cm}^{-3}$.

The electrical transport properties as a function of electron mean free path at different temperatures are displayed in Fig. 4-4 (a). At the room temperature, the greatest contribution to the conductivity comes from the electrons with mean free paths smaller than 37 nm, regarded as the maximum electron mean free path. As the temperature is lifted, the maximum mean free path decreases. We also realize that the height of the peak in normalized truncated Seebeck coefficient decreases when temperature rises, as described in Fig. 4-4 (b). We refer to electron mean free path at different temperatures in Fig. 4-3. At room temperature, the mean free paths of electrons above and below the chemical potential contrast profoundly. At high temperatures, such contrast gradually becomes inconspicuous, causing lowered peak height in the normalized truncated Seebeck coefficient. In Fig. 4-4 (c), the maximum

normalized truncated power factor, is as high as 230 % at 300 K but the maximum is almost unity at 700 K. Compared with phonon mean free path profile in Fig.4-4 (d), the mean free paths of electrons that contribute the majority of the power factor are larger than phonons contributing the majority of the thermal conductivity at all temperatures.

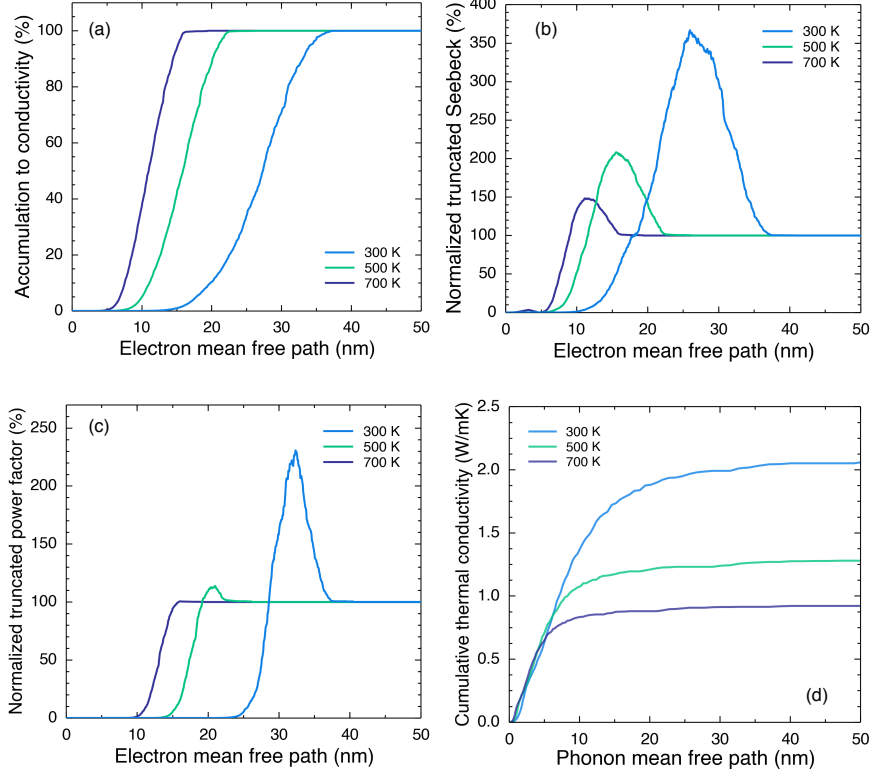


Figure 4-4: (a) The accumulated electrical conductivity with respect to electron mean free path. The normalized truncated (b) Seebeck coefficient and (c) power factor with respect to electron mean free path. (d) The accumulated lattice thermal conductivity with respect to phonon mean free path. The dopant concentration is $5.8 \times 10^{19} \text{ cm}^{-3}$.

The Fig. 4-5 (a) presents the conductivity as a function of temperature for different dopant concentrations, compared with La-doped PbTe from the experiment[54]. The decrease of the mobility versus temperature is mostly because electron-phonon scattering becomes stronger with an increase in temperature. Our calculation overall captures the correct trend both for mobility and conductivity. However, the calculated Seebeck coefficient in Fig. 4-5 (b) is largely underestimated above 400 K for

the lowest dopant concentration. As is known in PbTe, high temperatures flatten the band structure near the band edge, causing a larger effective mass[61], while in calculation, the band structure keeps unchanged. This also leads to the discrepancy between the calculation of the calculated power factor and experimental results. The band gap and the alignment of different valleys are function of temperature in reality that can also alter the Seebeck coefficient, yet not captured by our constant-band-gap calculation. In addition, the experiment demonstrates that for La-doped PbTe when the Hall carrier concentration is above $6 \times 10^{19} \text{ cm}^{-3}$, there is a deviation from valence counting rule that each dopant atom provides one carrier[54]. We believe this further contributes the differences between our calculation and experiment at $9.4 \times 10^{19} \text{ cm}^{-3}$.

Since our first-principles calculation of electron-phonon scattering is parameter-free, we can calculate the electronic thermal conductivity at different temperatures for different dopant concentrations instead of relying on the Wiedemann-Franz law, shown in Fig. 4-5 (c). For high dopant concentrations, even though the chemical potential is being lowered towards the band minimum as the temperature is elevated, the chemical potential is still close to the conduction band. For the low carrier concentration case ($4.3 \times 10^{-18} \text{ cm}^{-3}$), the chemical potential is closer to the middle of the band gap. With increasing temperature, holes start to contribute to the electronic thermal conductivity since the bipolar transport becomes noticeable, which corresponds to the increase above 400 K. Note that at the high carrier concentration ($5.8 \times 10^{-19} \text{ cm}^{-3}$), the thermal conductivity is lower than the electronic thermal conductivity which marks the significance to accurately estimate the electronic thermal conductivity.

In the experiment, it's usually difficult to distinguish the bipolar thermal conductivity from the measured thermal conductivity. However, the bipolar thermal conductivity can be explicitly calculated from our DFT calculation, shown in Fig. 4-5 (d). A noticeable increase is only observed in the low concentration of $4.3 \times 10^{-18} \text{ cm}^{-3}$ above 400 K. The total thermal conductivity is shown in Fig. 4-5 (e). Our results in Fig. 4-5 (c) indicates that the increase of electronic thermal conductivity leads to an increase of the total thermal conductivity. However, the experiment only shows

a minor increase. We believe this is due to fact that the calculation does not capture the increased effective mass and temperature-dependent band gap above 400 K. The figure of merit at high temperature is largely underestimated demonstrated in Fig. 4-5 (f), again, due to the inaccurate band structure at high temperatures. For the highest dopant concentration, both calculation and experiment show a monotonic increase with temperature because the the chemical potential is still far from being at the middle of the band gap so that the bipolar effect is insignificant.

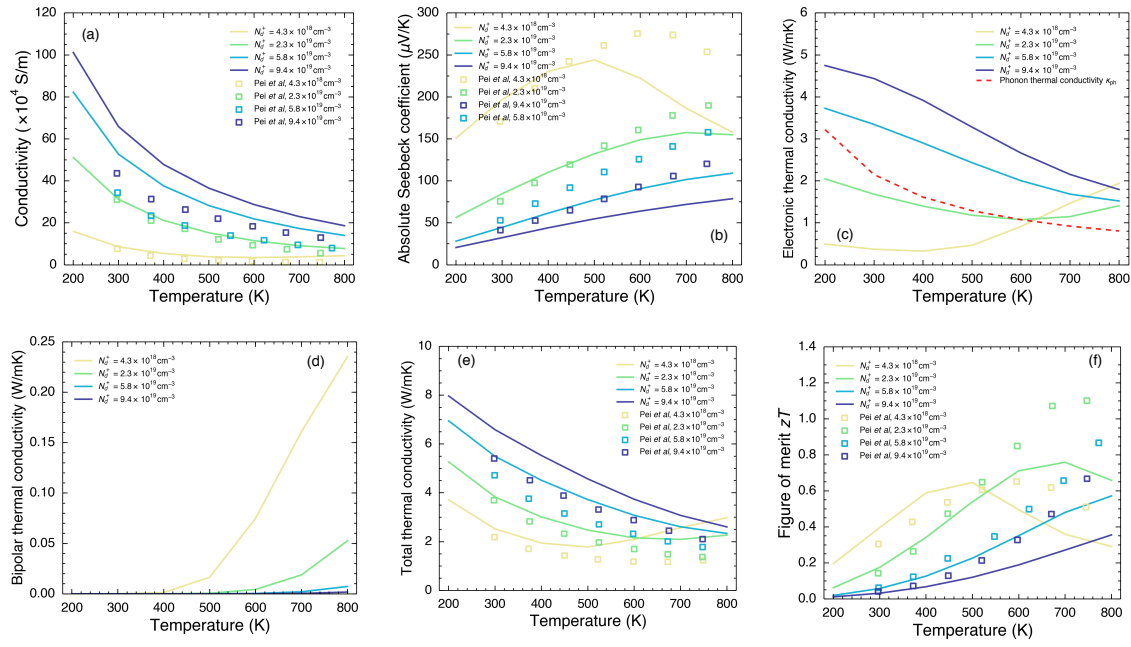


Figure 4-5: (a) The conductivity, (b) the Seebeck coefficient, (c) the electronic thermal conductivity compared with phonon thermal conductivity, (d) the bipolar thermal conductivity, (e) the total thermal conductivity and (f) the figure of merit zT of PbTe as a function of temperature for different ionized donor concentrations.

The squares are experimental results from Ref.[54]

4.2 Weakly isotropic scattering rates in PbTe

In Appendix B, we have demonstrated the strong anisotropy of the effective mass in PbTe. The anisotropic effective mass is generally believed to be beneficial for thermoelectric performance. On one hand, the light mass (typically transverse effective mass) implies a high mobility. On the other hand, the heavy mass (typical

longitudinal effective mass) indicates a high Seebeck coefficient. However, such argument is based on the constant relaxation time approximation where the details of electron-phonon scattering is lacked. Therefore, the argument to attribute the origin of high mobility and high Seebeck at the same time to the anisotropic band structure is never fully justified. In Fig. 4-6, we plot the electron-phonon scattering rate as a function of the electron wavevector. We find that the for low-energy electrons near the band minimum, the scattering rate is dominated by electron-LO-phonon scattering. For high-energy electrons at $L \rightarrow \Gamma$ path, the electron-acoustic-phonon scattering is much more significant than the scattering between electrons and phonons with other polarizations. Most interestingly, we not only clearly see the asymmetry of effective mass at the band edge, but find that for electrons with energy within the range of 0.5 eV above the conduction band minimum, the scattering rate is almost isotropic. In other words, the scattering rate profile at least does not compromise the benefits of the anisotropic band structure.

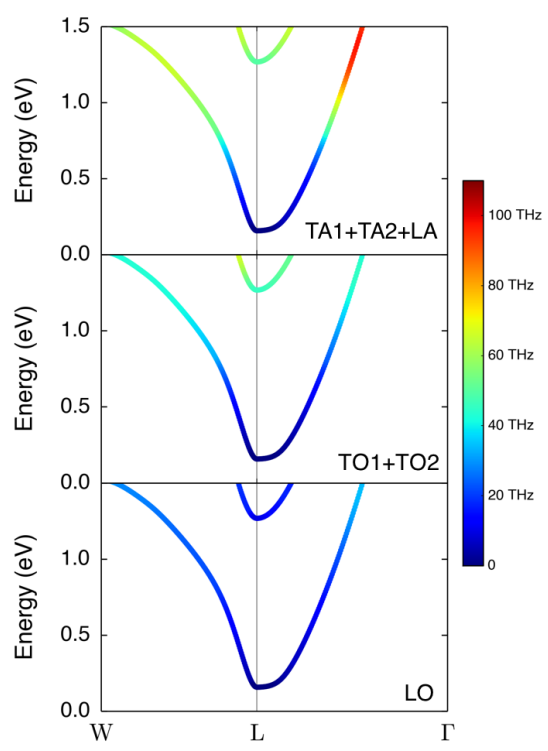


Figure 4-6: Electron-phonon scattering rates for different phonon polarizations mapped into the electron band structure. $L \rightarrow W$ is light-mass direction and $L \rightarrow \Gamma$ is the heavy mass-direction.

Chapter 5

Summary and future work

5.1 Summary

We have discussed the challenges in enhancing the performances of thermoelectric materials and shown that making bulk nanostructured thermoelectric materials boosts figure of merit zT significantly. We have identified the critical role that computational modeling using first principles plays in guiding experimentalists to choose the best grain size to optimize the figure of merit. Previous efforts in using *ab initio* method to extract the mean free path of phonons in PbTe inspires to study the electron dynamics to complete the spectrum of thermoelectric transport properties in PbTe from first principles. The key information we need to study electron transport in PbTe is the electron-phonon coupling matrix. However, the computational cost to calculate the electron-phonon coupling matrix is unacceptable. Thus, we introduce the method of electron-phonon Wannier interpolation which takes advantage of the localized feature of the electron-phonon vertex in the Wannier representation and reduces the computational cost dramatically. We have also derived the form of the screened Fröhlich interaction to properly take into account the effect of the dipole field associated LO phonon in doped semiconductors.

We have studied the electron-phonon interaction in *n*-type PbTe from first-principles calculation and obtain the electron-phonon scattering rates and electron mean free paths at different temperatures. The LO phonon in PbTe plays an important role

in determining the lifetime of electrons. The electron mean free path as a function of energy follows almost the same trend as the relaxation time because of the weak energy dependence of group velocity. This makes the electron mean free path decrease monotonically with energy. The screening effect at high carrier concentrations weakens the LO-TO splitting for phonons and reduces the POP scattering especially for low-energy electron. It also shifts the mean free path distribution towards higher values whilst the integrated transport properties are slightly changed. At elevated temperatures, the scattering rates scale with T and the electron mean free path distribution is shifted towards lower values.

The truncated Seebeck coefficient and power factor as a function of electron mean free path is not a monotonically increasing function. There exists a critical mean free path, corresponding to that of the electrons at the chemical potential, below which electrons contribute positively to the Seebeck coefficient while longer-mean-free-path electrons contribute negatively to the Seebeck coefficient. More interestingly, unlike in silicon, the electron mean free paths in PbTe are not significantly smaller than the mean free paths of most of the phonons. This inspires us to further investigate the scattering by interfaces both for electrons and phonons to rigorously and comprehensively answer the question if nanostructuring works better in silicon than in PbTe.

5.2 Future work

5.2.1 Symmetry analysis on the electron-phonon coupling matrix

In Sec. 3.3, we show the electron-phonon coupling matrix as a function of the electron wavevector and phonon wavevector. At certain high-symmetry point for electrons and phonons, the electron-phonon coupling matrix is exactly zero potentially due to symmetry restriction. Also, for certain \mathbf{k} and \mathbf{q} , the electron-phonon coupling strength is strong yet the strong coupling does not contribute to the scattering process due to

large energy mismatch of electron initial and final states compared with the available phonon energy. How to bridge the symmetry of the electron-phonon coupling matrix and good thermoelectric properties is unknown. In addition to that, the $\text{Pb}_x\text{Sn}_{1-x}\text{Te}$ alloy is known as a topological crystalline insulator (TCI) whose surface state is free of backscattering. However, at the room temperature, the surface states can still be scattered by phonons, which limits the practical application of TCI. Understanding the electron-phonon coupling for those surface states is crucial.

5.2.2 Scattering by the grain boundary

Bulk nanostructuring creates a high density of grain boundaries which induces scattering for electrons. People have proposed Wentzel-Kramers-Brillouin (WKB) transmission model[49], thermionic emission (thermionic field emission in space-charge potential) model[11], and Landauer dipole theory[34][79], etc. However, a parameter-free formalism using first principles to study the electron transport across the interface is still lacking. Yazyev and Louie proposed the theory of charge transport in two-dimensional polycrystalline graphene and generalized three classes of interfaces based on *ab initio* calculations[76]. It would be interesting to generalize the three-dimensional interfacial transport theory as such theory is much more useful in practical materials.

Appendix A

Lindhard dielectric function

Response function for electrons. Complete time-dependent Hamiltonian for electron,

$$H = H_0 + H'(t) \quad (\text{A.1})$$

The perturbation due to displacements of ions writes,

$$H'(t) = \sum_j O_j(t) A_j(t) \quad (\text{A.2})$$

The observable quantity out of equilibrium,

$$\langle O_j(t) \rangle_{n.e.} = \langle O_j(t) \rangle + \int d\tau \chi_{ji}(t - \tau) A_i(\tau) \quad (\text{A.3})$$

where,

$$\langle O_j(\omega) \rangle = \sum_i \chi_{ji}(\omega) A_i(\omega) \quad (\text{A.4})$$

Now take electron gas linearly coupled with a time-dependent external potential $V_{ext}(\mathbf{r}, t)$ as an example,

$$H(t) = H_0 + \int V_{ext}(\mathbf{r}, t) n(\mathbf{r}) d\mathbf{r} \quad (\text{A.5})$$

where $n(\mathbf{r}) = \sum_i \delta(\mathbf{r} - \mathbf{r}_i)$ is the density operator. Note that we assume the field $V_{ext}(\mathbf{r}, t)$ vanishes for t earlier than t_0 . For $t < t_0$, the system is assumed to be at thermal equilibrium with a huge thermal reservoir. The population of different state is defined by,

$$P_n = \frac{e^{-\beta E_n}}{Z} \quad (\text{A.6})$$

where $Z = \sum_n e^{-\beta E_n}$ is the partition function in a canonical ensemble and the E_n is the eigenvalue corresponding to the eigenfunction $|\phi_n\rangle$. Here, we implicitly apply adiabatic assumption where the time evolutions that are fast on the scale of the thermal equilibration time[19].

In Schrödinger picture, the solution for eigenvector is

$$|\phi_n(t)\rangle = U(t, t_0) |\phi_n(t_0)\rangle \quad (\text{A.7})$$

where $U(t, t_0)$ is the time-evolution operator,

$$U(t, t_0) = e^{-\frac{i}{\hbar} H(t-t_0)} U_V(t, t_0) \quad (\text{A.8})$$

where the operator $U_V(t, t_0)$ obeys,

$$i\hbar \frac{\partial}{\partial t} U_V(t, t_0) = V_{ext}(t) n(t-t_0) U_V(t, t_0) \quad (\text{A.9})$$

The time-dependent operator,

$$n(t) = e^{\frac{i}{\hbar} H_0 t} n(t_0) e^{-\frac{i}{\hbar} H_0 t} \quad (\text{A.10})$$

The first-order expansion of U_V is,

$$U_V(t, t_0) = 1 - \frac{i}{\hbar} \int_{t_0}^t n(t' - t_0) V_{ext}(t') dt' \quad (\text{A.11})$$

Then the time-evolution operator writes,

$$U(t, t_0) = e^{-\frac{i}{\hbar}H_0(t-t_0)} \left[1 - \frac{i}{\hbar} \int_{t_0}^t n(t' - t_0) V_{ext}(t') dt' \right] \quad (\text{A.12})$$

Observable $A(t)$

$$\langle A(t) \rangle = \sum_n P_n \langle \phi_n(t) | A | \phi_n(t) \rangle \quad (\text{A.13})$$

The deviation is,

$$\langle A \rangle - \langle A_0 \rangle = -\frac{i}{\hbar} \int_{t_0}^t \langle [A(t), n(t')] \rangle_0 V_{ext}(t') dt' \quad (\text{A.14})$$

Note that,

$$\langle [A(t), n(t')] \rangle_0 = \langle [A(\tau), n(0)] \rangle_0 \quad (\text{A.15})$$

where $\tau = t - t' > 0$, and the retarded linear response function (susceptibility) is,

$$\chi_{An}(\tau) = -\frac{i}{\hbar} \Theta(\tau) \langle [A(\tau), n] \rangle_0 \quad (\text{A.16})$$

Apparently, $\Theta(\tau) = 0$ for $\tau < 0$ but $\Theta(\tau) = 1$ for $\tau > 0$. Then,

$$\langle A(t) \rangle_1 = \langle A(t) \rangle - \langle A(0) \rangle = \int_0^{t-t_0} \chi_{An}(\tau) V_{ext}(t-\tau) d\tau \quad (\text{A.17})$$

Add a periodic time dependence to the perturbation as,

$$V_{ext}(t) = V_\omega e^{-i\omega t} + \text{c.c.} = \int_{-\infty}^{\infty} V(\omega) e^{-i\omega t} \frac{d\omega}{2\pi} \quad (\text{A.18})$$

where

$$V(\omega) = \int_{-\infty}^{\infty} V_{ext}(t) e^{i\omega t} dt \quad (\text{A.19})$$

To make sure $V_{ext}(t) = 0$ when $t = -\infty$,

$$V_{ext}(t) = V_\omega e^{-i(\omega+i\eta)t} + \text{c.c.} \quad (\text{A.20})$$

Rewrite Eq. A.17 as,

$$\langle A(t) \rangle_1 = \langle A(\omega) \rangle_1 e^{-i(\omega+i\eta)t} + \text{c.c.} \quad (\text{A.21})$$

where,

$$A_1(\omega) = \chi_{An}(\omega) V_\omega \quad (\text{A.22})$$

and

$$\chi_{An}(\omega) = -\frac{i}{\hbar} \lim_{\eta \rightarrow 0} \int_0^\infty \langle [A(\tau), n] \rangle e^{i(\omega+i\eta)\tau} d\tau \quad (\text{A.23})$$

The commutator,

$$\langle [A(\tau), B] \rangle_0 = \sum_{m,n} P_m (e^{i\omega_{mn}\tau} A_{mn} B_{nm} - e^{i\omega_{nm}\tau} B_{mn} A_{nm}) = \sum_{m,n} (P_m - P_n) e^{i\omega_{mn}\tau} A_{mn} B_{nm} \quad (\text{A.24})$$

The response function,

$$\chi_{AB}(\omega) = \frac{1}{\hbar} \sum_{nm} \frac{P_m - P_n}{\omega - \omega_{nm} + i\eta} A_{mn} B_{nm}. \quad (\text{A.25})$$

Separate Eq. A.25,

$$\lim_{\eta \rightarrow 0} \frac{1}{\omega - y + i\eta} = \mathcal{P} \frac{1}{\omega - y} - i\pi \delta(\omega - y), \quad (\text{A.26})$$

where \mathcal{P} is the Cauchy principle value.

Polarization of electrons.

$$U_{ext}(\mathbf{r}, t) = U_{ext}(\mathbf{q}, \omega) e^{i(\mathbf{q} \cdot \mathbf{r} - \omega t)} + \text{c.c.} \quad (\text{A.27})$$

where the $U_{ext}(\mathbf{q}, \omega) = \epsilon(\mathbf{q}, \omega) U(\mathbf{q}, \omega)$. Note the real part and imaginary part of dielectric function obey the Kramers-Kronig relations,

$$\epsilon_1(\mathbf{q}, \omega) = 1 + \frac{1}{\pi} \mathcal{P} \int_{-\infty}^{\infty} \frac{\epsilon_2(\mathbf{q}, \omega')}{\omega' - \omega} d\omega' \quad (\text{A.28})$$

Meanwhile,

$$\epsilon_2(\mathbf{q}, \omega) = -\frac{1}{\pi} \mathcal{P} \int_{-\infty}^{\infty} \frac{\epsilon_1(\mathbf{q}, \omega') - 1}{\omega' - \omega} d\omega' \quad (\text{A.29})$$

Equivalently,

$$\epsilon_1(\mathbf{q}, \omega) = 1 + \frac{2}{\pi} \mathcal{P} \int_0^{\infty} \omega' \frac{\epsilon_2(\mathbf{q}, \omega')}{\omega'^2 - \omega^2} d\omega' \quad (\text{A.30})$$

Imaginary part,

$$\epsilon_2(\mathbf{q}, \omega) = -\frac{2\omega}{\pi} \mathcal{P} \int_0^{\infty} \frac{\epsilon_1(\mathbf{q}, \omega') - 1}{\omega'^2 - \omega^2} d\omega' \quad (\text{A.31})$$

Now we try to derive the longitudinal dielectric function. One-electron Hamiltonian (Ref. [25], pp.320),

$$H_0 = -\frac{\hbar^2 \nabla^2}{2m} + V(\mathbf{r}) \quad (\text{A.32})$$

The perturbation of the potential energy,

$$U(\mathbf{r}, t) = U_0 e^{i(\mathbf{q} \cdot \mathbf{r} - \omega t)} + \text{c.c.} \quad (\text{A.33})$$

The electrostatic potential corresponding to the perturbation is $\phi(\mathbf{r}, t) = \frac{U(\mathbf{r}, t)}{-e}$. The electric field, is,

$$\mathbf{E} = -\nabla \phi = \frac{\nabla U(\mathbf{r}, t)}{e} = \frac{iqU_0}{e} e^{i(\mathbf{q} \cdot \mathbf{r} - \omega t)} \hat{\mathbf{e}} + \text{c.c.} \quad (\text{A.34})$$

The Hamiltonian becomes,

$$H = H_0 + U_0 e^{i(\mathbf{q} \cdot \mathbf{r} - \omega t)} + U_0^* e^{-i(\mathbf{q} \cdot \mathbf{r} - \omega t)} \quad (\text{A.35})$$

The transition probability based on the Fermi's golden rule,

$$\begin{aligned} P_{\beta \leftarrow \alpha} &= \frac{2\pi}{\hbar} |\langle \phi_\beta | U_0 e^{i\mathbf{q} \cdot \mathbf{r}} | \phi_\alpha \rangle|^2 \delta(E_\beta - E_\alpha - \hbar\omega) \\ P_{\alpha \leftarrow \beta} &= \frac{2\pi}{\hbar} |\langle \phi_\alpha | U_0 e^{-i\mathbf{q} \cdot \mathbf{r}} | \phi_\beta \rangle|^2 \delta(E_\alpha - E_\beta + \hbar\omega) \end{aligned} \quad (\text{A.36})$$

The transition rate,

$$\begin{aligned}
W(\mathbf{q}, \omega) &= g_s \frac{2\pi}{\hbar} \sum_{\alpha\beta} |\langle \phi_\beta | U_0 e^{i\mathbf{q}\cdot\mathbf{r}} | \phi_\alpha \rangle|^2 \\
&\times \left[\delta(E_\beta - E_\alpha - \hbar\omega) f(E_\alpha)(1 - f(E_\beta)) - \delta(E_\beta - E_\alpha + \hbar\omega) f(E_\beta)(1 - f(E_\alpha)) \right]
\end{aligned} \tag{A.37}$$

where g_s is the spin degeneracy. The energy dissipated per unit time in volume V is,

$$\begin{aligned}
\int_V \mathbf{J} \cdot \mathbf{E} d\mathbf{r} &= \int_V [\sigma(\mathbf{q}, \omega) E_0 e^{i(\mathbf{q}\cdot\mathbf{r}-\omega t)} + \text{c.c.}] [E_0 e^{i(\mathbf{q}\cdot\mathbf{r}-\omega t)} + \text{c.c.}] d\mathbf{r} \\
&= 2\sigma_1(\mathbf{q}, \omega) \frac{q^2}{e^2} |U_0|^2 V = \hbar\omega W(\mathbf{q}, \omega)
\end{aligned} \tag{A.38}$$

The current density satisfies,

$$\frac{\partial \mathbf{D}}{\partial t} = \frac{\partial \mathbf{E}}{\partial t} + 4\pi \mathbf{J} \tag{A.39}$$

where $\mathbf{D} = \epsilon \mathbf{E}$ and $\mathbf{J} = \sigma \mathbf{E}$

$$\sigma_1(\mathbf{q}, \omega) = \frac{1}{2} \frac{e^2}{q^2} \frac{\hbar\omega W(\mathbf{q}, \omega)}{|U_0|^2 V} \tag{A.40}$$

The imaginary part of dielectric constant is,

$$\begin{aligned}
\epsilon_2(\mathbf{q}, \omega) &= \frac{4\pi}{\omega} \sigma_1(\mathbf{q}, \omega) = \frac{2\pi\hbar e^2}{q^2} \frac{1}{V} \frac{W(\mathbf{q}, \omega)}{|U_0|^2} \\
&= \frac{4\pi^2 e^2}{q^2} g_s \sum_{\alpha\beta} |\langle \phi_\beta | e^{i\mathbf{q}\cdot\mathbf{r}} | \phi_\alpha \rangle|^2 \\
&\times \left[\delta(E_\beta - E_\alpha - \hbar\omega) f(E_\alpha)(1 - f(E_\beta)) - \delta(E_\beta - E_\alpha + \hbar\omega) f(E_\beta)(1 - f(E_\alpha)) \right]
\end{aligned} \tag{A.41}$$

Using the Kramers-Kronig relation, we have,

$$\begin{aligned}\epsilon_1(\mathbf{q}, \omega) &= 1 + \frac{1}{\pi} \mathcal{P} \int_{-\infty}^{\infty} \frac{\epsilon_2(\mathbf{q}, \omega')}{\omega' - \omega} d\omega' \\ &= 1 + \frac{4g_s \pi e^2}{q^2} \frac{1}{V} \sum_{\alpha\beta} \left[\frac{|\langle \phi_\beta | e^{i\mathbf{q}\cdot\mathbf{r}} | \phi_\alpha \rangle|^2}{E_\beta - E_\alpha - \hbar\omega - i\eta} f(E_\alpha)(1 - f(E_\beta)) \right. \\ &\quad \left. - \frac{|\langle \phi_\beta | e^{i\mathbf{q}\cdot\mathbf{r}} | \phi_\alpha \rangle|^2}{E_\beta - E_\alpha + \hbar\omega - i\eta} f(E_\beta)(1 - f(E_\alpha)) \right]\end{aligned}\quad (\text{A.42})$$

Long wavelength limit. When $\mathbf{q} \rightarrow 0$, the matrix element,

$$\begin{aligned}\langle \phi_\beta | e^{i\mathbf{q}\cdot\mathbf{r}} | \phi_\alpha \rangle &= i\mathbf{q} \cdot \langle \phi_\beta | \mathbf{r} | \phi_\alpha \rangle \\ &= \frac{\hbar}{m} \frac{\mathbf{q} \cdot \langle \phi_\beta | \mathbf{p} | \phi_\alpha \rangle}{E_\beta - E_\alpha}\end{aligned}\quad (\text{A.43})$$

due to equality,

$$[H_0, \mathbf{r}] = -i\hbar\mathbf{p}/m. \quad (\text{A.44})$$

$$\begin{aligned}\epsilon(0, \omega) &= 1 + \frac{4g_s \pi e^2}{m^2} \frac{1}{V} \sum_{\alpha\beta} \frac{|\langle \phi_\beta | \hat{\mathbf{e}} \cdot \mathbf{p} | \phi_\alpha \rangle|^2}{[(E_\beta - E_\alpha)/\hbar]^2} \left[\frac{f(E_\alpha)(1 - f(E_\beta))}{E_\beta - E_\alpha - \hbar\omega - i\eta} - \frac{f(E_\beta)(1 - f(E_\alpha))}{E_\beta - E_\alpha + \hbar\omega - i\eta} \right]\end{aligned}\quad (\text{A.45})$$

Static limit. The static limit considering $E(\mathbf{k}) = \hbar^2 k^2 / 2m$ and free-electron gas,

$$\epsilon(q) = 1 + \frac{4\pi g_s e^2}{q^2} \frac{1}{V} \sum_{\mathbf{k}} \frac{f_{\mathbf{k}} - f_{\mathbf{k}+\mathbf{q}}}{E(\mathbf{k} + \mathbf{q}) - E(\mathbf{k}) - i\eta} \quad (\text{A.46})$$

which is the so-called Lindhard dielectric function for the free electron gas. By some treatment, the Lindhard dielectric function writes[45],

$$\epsilon(q) = 1 + \frac{1}{2} \frac{k_{TF}^2}{q^2} + \frac{1}{2} \frac{k_{TF}^2}{q^2} \frac{k_F}{q} \left(1 - \frac{q^2}{4k_F^2} \right) \ln \left| \frac{2k_F + q}{2k_F - q} \right| \quad (\text{A.47})$$

Appendix B

Anisotropic effective mass of electrons

Near the band edge, the electronic energy can be expanded by $\epsilon_{n\mathbf{k}} = \epsilon_0 + \hbar^2 m_{ij}^{*-1} \Delta k_i \Delta k_j / 2$, where ϵ_0 is band extreme and \mathbf{k}_i is the wavevector in Cartesian coordinate. The inverse of the effective mass is given by,

$$m_{ij}^{*-1} = \frac{2}{\hbar^2} \frac{\partial^2 \epsilon_{nk}}{\partial k_i \partial k_j} \quad (\text{B.1})$$

To calculate the effective mass tensor, the knowledge of eigenvalues of electronic states near the band extreme is required. A non-self-consistent calculation is performed on a $5 \times 5 \times 5$ uniform k -mesh centered at the band minimum (in this work it's at L point in the first Brillouin zone both for conduction band and valence band). Then a two-dimensional five-point stencil under a finite difference approximations is chosen for the calculation of the second derivative of energy with respect to wavevector. The coefficients used in the calculation are as follows[2],

$$\begin{aligned} \frac{\partial^2 \epsilon_{n\mathbf{k}}}{\partial k_i^2} &\approx \frac{-E_{-2} + 16E_{-1} - 30E_0 + 16E_1 - E_2}{12\Delta^2} \sim O(\Delta^4) \\ \left. \frac{\partial^2 \epsilon_{n\mathbf{k}}}{\partial k_i \partial k_j} \right|_{i \neq j} &\approx \frac{1}{600\Delta^2} \left[44(E_{2,2} + E_{-2,-2} + E_{2,-2} + E_{-2,2}) \right. \\ &\quad - 63(E_{1,-2} + E_{-1,2} + E_{-2,1} + E_{2,-1}) \\ &\quad + 63(E_{-1,-2} + E_{1,2} + E_{-2,-1} + E_{2,1}) \\ &\quad \left. + 74(E_{-1,-1} + E_{1,1} + E_{-1,1} + E_{1,-1}) \right] \sim O(\Delta^4) \end{aligned} \quad (\text{B.2})$$

where Δ is the spacing of the k mesh and calculated E_{ij} the energy on the k point with a offset of $i \times \Delta$ in k_i direction and $j \times \Delta$ in k_j direction.

We then take the inverse of m_{ij}^{*-1} to obtain effective mass tensor, which is a 2nd-order tensor. The principle values of a 2nd-order tensor is the eigenvalues of the tensor. Those principle values are actually referred to as the so-called longitudinal effective mass and transverse electron/hole effective mass. Meanwhile, the principle axes is determined by the eigenvectors. The eigenvectors *i.e.* the principal axes of the effective mass tensor of PbTe is as follows. For valence band,

$$\mathbf{e}_1 = \begin{pmatrix} 0.577 \\ -0.577 \\ -0.577 \end{pmatrix}, \quad \mathbf{e}_2 = \begin{pmatrix} -0.049 \\ -0.730 \\ 0.681 \end{pmatrix}, \quad \mathbf{e}_3 = \begin{pmatrix} -0.815 \\ -0.365 \\ -0.450 \end{pmatrix}. \quad (\text{B.3})$$

For conduction band,

$$\mathbf{e}_1 = \begin{pmatrix} 0.811 \\ 0.487 \\ 0.324 \end{pmatrix}, \quad \mathbf{e}_2 = \begin{pmatrix} 0.095 \\ -0.655 \\ 0.750 \end{pmatrix}, \quad \mathbf{e}_3 = \begin{pmatrix} -0.577 \\ 0.577 \\ 0.577 \end{pmatrix}. \quad (\text{B.4})$$

The calculated principal values of the effective mass tensor is shown in Table B.2, where m_{vt}^* and m_{vl}^* are the transverse and longitudinal effective of valence band and m_{ct}^* and m_{cl}^* for conduction band. We notice that the experiment (under 4 K tem-

Table B.1: The longitudinal and transverse effective mass of PbTe from calculation and experiment[31]

	m_{vt}^*	m_{vl}^*	m_{ct}^*	m_{cl}^*
Calculation	-0.190	-0.466	0.089	0.185
Experiment	-0.022 ± 0.003	-0.31 ± 0.05	0.024 ± 0.003	0.24 ± 0.05

perature) shows a strong mass anisotropy ($m_l/m_t \geq 10$ both for conduction band minimum and valence band maximum), which is not captured by the first-principles calculation. This might be due to the fact that the LDA pseudopotential cannot produce an accurate band edge profile and more advanced calculation scheme, *e.g.*

quasiparticle self-consistent GW , should be adopted[68]. In fact, the effective mass of PbTe is highly sensitive to temperature[42]. Since we focus on transport properties at and above room temperature, it's important to compare with measurement of the effective mass at room temperature. The density of states effective mass and conductivity are closely related to the transport properties, given by,

$$m_{\text{DOS}}^* = (m_l^* m_t^{*2})^{1/3} \quad (\text{B.5})$$

$$m_{\text{cond}}^* = \frac{3}{1/m_l^* + 2/m_t^*} \quad (\text{B.6})$$

Table B.2: The DOS and conductivity effective mass of PbTe from calculation and experiment[42]

	$m_{v,\text{DOS}}^*$	$m_{v,\text{cond}}^*$	$m_{c,\text{DOS}}^*$	$m_{c,\text{cond}}^*$
Calculation	-0.256	-0.237	0.114	0.108
Experiment (300 K)	-0.250	-0.110	0.300	0.103

Appendix C

Phonon thermal conductivity from first principles

The heat flux by phonons is caused by the deviation of the distribution function from equilibrium in an isotropic material[7],

$$\mathbf{J}_{ph} = \frac{1}{\Omega N_{\nu\mathbf{q}}} \sum_{\nu\mathbf{q}} \hbar\omega_{\nu\mathbf{q}} \mathbf{v}_{\nu\mathbf{q}} (n_{\nu\mathbf{q}} - n_{\nu\mathbf{q},0}). \quad (\text{C.1})$$

Considering the Fourier's law $\mathbf{J}_{ph} = -\kappa_{ph} \nabla_{\mathbf{r}} T$, we find that the expression for phonon thermal conductivity from linearized Boltzmann transport equation under the relaxation time approximation is,

$$\kappa_{ph}^{\alpha\beta} = \frac{1}{\Omega N_{\nu\mathbf{q}}} \sum_{\nu\mathbf{q}} \frac{(\hbar\omega_{\nu\mathbf{q}})^2}{k_B T^2} n_{\nu\mathbf{q}} (n_{\nu\mathbf{q}} + 1) \mathbf{v}_{\nu\mathbf{q}}^\alpha \mathbf{v}_{\nu\mathbf{q}}^\beta \tau_{\nu\mathbf{q}}, \quad (\text{C.2})$$

where $N_{\mathbf{q}}$ is number of the q point. The calculation of the thermal conductivity requires the phonon dispersion relation, which contains the information of phonon frequency and group velocity. We also need to calculate the relaxation time and this can be calculated by,

$$\frac{1}{\tau_{\nu\mathbf{q}}} = \frac{1}{N_{\mathbf{q}}} \left(\sum_{\substack{\nu'\nu'' \\ \mathbf{q}'\mathbf{q}''}} {}^+ \Gamma_{\mathbf{q}\mathbf{q}'\mathbf{q}''}^{\nu\nu'\nu''} + \frac{1}{2} \sum_{\substack{\nu'\nu'' \\ \mathbf{q}'\mathbf{q}''}} {}^- \Gamma_{\mathbf{q}\mathbf{q}'\mathbf{q}''}^{\nu\nu'\nu''} \right). \quad (\text{C.3})$$

The term ${}^{\pm}\Gamma_{\mathbf{q}\mathbf{q}'\mathbf{q}''}^{\nu\nu'\nu''}$ corresponds to the phonon absorption/emission process,

$$\begin{aligned} {}^{\pm}\Gamma_{\mathbf{q}\mathbf{q}'\mathbf{q}''}^{\nu\nu'\nu''} &= \frac{\hbar\pi}{4\omega_{\nu\mathbf{q}}\omega_{\nu'\mathbf{q}'}\omega_{\nu\mathbf{q}''}} \\ &\times \left| {}^{\pm}V_{\mathbf{q}\mathbf{q}'\mathbf{q}''}^{\nu\nu'\nu''} \right|^2 \begin{bmatrix} n_{\nu'\mathbf{q}'} - n_{\nu''\mathbf{q}''} \\ n_{\nu'\mathbf{q}'} + n_{\nu''\mathbf{q}''} + 1 \end{bmatrix} \delta(\omega_{\nu\mathbf{q}} \pm \omega_{\nu'\mathbf{q}'} - \omega_{\nu''\mathbf{q}''}), \end{aligned} \quad (\text{C.4})$$

where ${}^{\pm}V_{\mathbf{q}\mathbf{q}'\mathbf{q}''}^{\nu\nu'\nu''}$ is the scattering matrix element. To calculate the thermal conductivity, we use a cubic supercell that contains 64 atoms to obtain scattering matrix in the formalism proposed by Ref.[14].

Bibliography

- [1] *We adopt rigid band approximation and shift the whole conduction bands relative to the valence bands to match the experimental band gap at different temperature. Note the band gap of lead telluride turns from direct into indirect above 400 K, which is missed in our treatment. In fact, we make sure the band gap in the calculation consistent with experimental values although the valley alignment might be inaccurate. And we find such treatment gives similar transport properties as a function of temperature, compared with the constant-band-gap calculation in the main text.*
- [2] Milton Abramowitz and Irene A Stegun. *Handbook of mathematical functions: with formulas, graphs, and mathematical tables*, volume 55. Courier Corporation, 1964.
- [3] J. Bardeen and W. Shockley. Deformation potentials and mobilities in non-polar crystals. *Phys. Rev.*, 80(1):72–80, 1950.
- [4] Stefano Baroni, Paolo Giannozzi, and Andrea Testa. GreenâŽs-function approach to linear response in solids. *Physical Review Letters*, 58(18):1861, 1987.
- [5] Kristian Berland and Clas Persson. Enabling accurate first-principle calculations of electronic properties with a corrected $k \cdot p$ scheme. *Computational Materials Science*, 134:17–24, 2017.
- [6] Kanishka Biswas, Jiaqing He, Ivan D Blum, Chun-I Wu, Timothy P Hogan, David N Seidman, Vinayak P Dravid, and Mercouri G Kanatzidis. High-performance bulk thermoelectrics with all-scale hierarchical architectures. *Nature*, 489(7416):414–418, sep 2012.
- [7] D. A. Broido, A. Ward, and N. Mingo. Lattice thermal conductivity of silicon from empirical interatomic potentials. *Phys. Rev. B*, 72:014308, Jul 2005.
- [8] Gang Chen. *Nanoscale energy transport and conversion: a parallel treatment of electrons, molecules, phonons, and photons*. Oxford University Press, 2005.
- [9] Xin Chen, David Parker, and David J Singh. Importance of non-parabolic band effects in the thermoelectric properties of semiconductors. 3:3168, nov 2013.

- [10] W. Cochran, R. A. Cowley, G. Dolling, and M. M. Elcombe. The crystal dynamics of lead telluride. *Proceedings of the Royal Society of London A: Mathematical, Physical and Engineering Sciences*, 293(1435):433–451, 1966.
- [11] AW De Groot and Howard C Card. Charge emission from interface states at silicon grain boundaries by thermal emission and thermionic-field emission—part i: Theory. *IEEE Transactions on Electron Devices*, 31(10):1365–1369, 1984.
- [12] O Delaire, J Ma, K Marty, A F May, M A McGuire, M-H. Du, D J Singh, A Podlesnyak, G Ehlers, M D Lumsden, and B C Sales. Giant anharmonic phonon scattering in PbTe. *Nat Mater*, 10(8):614–619, aug 2011.
- [13] Mildred S Dresselhaus, Gang Chen, Ming Y Tang, RG Yang, Hohyun Lee, DZ Wang, ZF Ren, J-P Fleurial, and Pawan Gogna. New directions for low-dimensional thermoelectric materials. *Advanced Materials*, 19(8):1043–1053, 2007.
- [14] Keivan Esfarjani, Gang Chen, and Harold T. Stokes. Heat transport in silicon from first-principles calculations. *Phys. Rev. B*, 84:085204, Aug 2011.
- [15] Y Gelbstein, Z Dashevsky, and M P Dariel. Synthesis of n-type PbTe by powder metallurgy. In *Thermoelectr. 2001. Proc. ICT 2001. XX Int. Conf.*, pages 143–149. IEEE, 2001.
- [16] Paolo Giannozzi, Stefano Baroni, Nicola Bonini, Matteo Calandra, Roberto Car, Carlo Cavazzoni, Davide Ceresoli, Guido L Chiarotti, Matteo Cococcioni, Ismaila Dabo, Andrea Dal Corso, Stefano de Gironcoli, Stefano Fabris, Guido Fratesi, Ralph Gebauer, Uwe Gerstmann, Christos Gougoussis, Anton Kokalj, Michele Lazzeri, Layla Martin-Samos, Nicola Marzari, Francesco Mauri, Riccardo Mazzarello, Stefano Paolini, Alfredo Pasquarello, Lorenzo Paulatto, Carlo Sbraccia, Sandro Scandolo, Gabriele Sclauzero, Ari P Seitsonen, Alexander Smogunov, Paolo Umari, and Renata M Wentzcovitch. Quantum espresso: a modular and open-source software project for quantum simulations of materials. *Journal of Physics: Condensed Matter*, 21(39):395502, 2009.
- [17] Zachary M. Gibbs, Hyounghul Kim, Heng Wang, Robert L. White, Fivos Drymiotis, Massoud Kaviani, and G. Jeffrey Snyder. Temperature dependent band gap in pbx ($x = s, se, te$). *Applied Physics Letters*, 103(26):262109, 2013.
- [18] Zachary M Gibbs, Aaron LaLonde, and G Jeffrey Snyder. Optical band gap and the burstein–moss effect in iodine doped pbte using diffuse reflectance infrared fourier transform spectroscopy. *New Journal of Physics*, 15(7):075020, 2013.
- [19] Gabriele Giuliani and Giovanni Vignale. *Quantum theory of the electron liquid*. Cambridge university press, 2005.
- [20] Feliciano Giustino. Electron-phonon interactions from first principles. *Rev. Mod. Phys.*, 89(1):015003, feb 2017.

- [21] Feliciano Giustino, Marvin L. Cohen, and Steven G. Louie. Electron-phonon interaction using wannier functions. *Phys. Rev. B*, 76:165108, Oct 2007.
- [22] Xavier Gonze. Perturbation expansion of variational principles at arbitrary order. *Physical Review A*, 52(2):1086, 1995.
- [23] Xavier Gonze and Changyol Lee. Dynamical matrices, born effective charges, dielectric permittivity tensors, and interatomic force constants from density-functional perturbation theory. *Phys. Rev. B*, 55:10355–10368, Apr 1997.
- [24] Prashun Gorai, Vladan Stevanović, and Eric S Toberer. Computationally guided discovery of thermoelectric materials. *Nature Reviews Materials*, 2(9):natrevmats201753, 2017.
- [25] Giuseppe Grosso and Giuseppe Pastori Parravicini. *Solid State Physics (Second Edition)*. Academic Press, Amsterdam, second edition edition, 2014.
- [26] TC Harman, DL Spears, and MJ Manfra. High thermoelectric figures of merit in pbte quantum wells. *Journal of Electronic Materials*, 25(7):1121, 1996.
- [27] Jian He and Terry M Tritt. Advances in thermoelectric materials research: Looking back and moving forward. *Science*, 357(6358):eaak9997, 2017.
- [28] LD Hicks and Mildred S Dresselhaus. Effect of quantum-well structures on the thermoelectric figure of merit. *Physical Review B*, 47(19):12727, 1993.
- [29] LD Hicks and Mildred S Dresselhaus. Thermoelectric figure of merit of a one-dimensional conductor. *Physical review B*, 47(24):16631, 1993.
- [30] Egil A. Hylleraas. Über den grundterm der zweielektronenprobleme von h , he , li^+ , be^{++} usw. *Zeitschrift für Physik*, 65(3):209–225, Mar 1930.
- [31] L.R. Williams K.F. Cuff, M.R. Ellett, C.D. Kuglin. Phys. of Semiconductors. In M. Hulin, editor, *Proc. 7th Int. Conf.*, pages 667–684, Dunod, Paris, 1964.
- [32] W. Kohn and L. J. Sham. Self-Consistent Equations Including Exchange and Correlation Effects. *Physical Review*, 140(4A):A1133–A1138, 1965.
- [33] Yucheng Lan, Austin Jerome Minnich, Gang Chen, and Zhifeng Ren. Enhancement of thermoelectric figure-of-merit by a bulk nanostructuring approach. *Advanced Functional Materials*, 20(3):357–376, 2010.
- [34] Rolf Landauer. Spatial variation of currents and fields due to localized scatterers in metallic conduction. *IBM Journal of Research and Development*, 1(3):223–231, 1957.
- [35] Sangyeop Lee, Keivan Esfarjani, Tengfei Luo, Jiawei Zhou, Zhiting Tian, and Gang Chen. Resonant bonding leads to low lattice thermal conductivity. *Nat. Commun.*, 5:3525, apr 2014.

- [36] H. W. Leite Alves, A. R. R. Neto, L. M. R. Scolfaro, T. H. Myers, and P. D. Borges. Lattice contribution to the high dielectric constant of pbte. *Phys. Rev. B*, 87:115204, Mar 2013.
- [37] Wu Li, Jesús Carrete, Nabil A. Katcho, and Natalio Mingo. ShengBTE: a solver of the Boltzmann transport equation for phonons. *Comp. Phys. Commun.*, 185:1747–1758, 2014.
- [38] Bolin Liao, AA Maznev, Keith A Nelson, and Gang Chen. Photo-excited charge carriers suppress sub-terahertz phonon mode in silicon at room temperature. *Nature communications*, 7, 2016.
- [39] Bolin Liao, Bo Qiu, Jiawei Zhou, Samuel Huberman, Keivan Esfarjani, and Gang Chen. Significant reduction of lattice thermal conductivity by the electron-phonon interaction in silicon with high carrier concentrations: A first-principles study. *Phys. Rev. Lett.*, 114:115901, Mar 2015.
- [40] Te-Huan Liu, Jiawei Zhou, Bolin Liao, David J. Singh, and Gang Chen. First-principles mode-by-mode analysis for electron-phonon scattering channels and mean free path spectra in gaas. *Phys. Rev. B*, 95:075206, Feb 2017.
- [41] Mark Lundstrom. *Fundamentals of carrier transport*. Cambridge University Press, 2009.
- [42] Henry A Lyden. Temperature Dependence of the Effective Masses in PbTe. *Phys. Rev.*, 135(2A):A514–A521, jul 1964.
- [43] Georg K.H. Madsen and David J. Singh. Boltztrap. a code for calculating band-structure dependent quantities. *Computer Physics Communications*, 175(1):67 – 71, 2006.
- [44] Gerald D. Mahan. *Many-Particle Physics*. Springer US, Boston, MA, 2000.
- [45] Gerald D Mahan. *Many-particle physics*. Springer Science & Business Media, 2013.
- [46] J Martin, Li Wang, Lidong Chen, and GS Nolas. Enhanced seebeck coefficient through energy-barrier scattering in pbte nanocomposites. *Physical review B*, 79(11):115311, 2009.
- [47] Nicola Marzari and David Vanderbilt. Maximally localized generalized wannier functions for composite energy bands. *Phys. Rev. B*, 56:12847–12865, Nov 1997.
- [48] AB Migdal. Interaction between electrons and lattice vibrations in a normal metal. *Sov. Phys. JETP*, 7(6):996–1001, 1958.
- [49] VV Mitin. Contribution of light holes to thermionic field emission in si and ge. *Physical Review B*, 31(4):2584, 1985.

- [50] Hendrik J. Monkhorst and James D. Pack. Special points for brillouin-zone integrations. *Phys. Rev. B*, 13:5188–5192, Jun 1976.
- [51] Arash A Mostofi, Jonathan R Yates, Giovanni Pizzi, Young-Su Lee, Ivo Souza, David Vanderbilt, and Nicola Marzari. An updated version of wannier90: A tool for obtaining maximally-localised wannier functions. *Computer Physics Communications*, 185(8):2309–2310, 2014.
- [52] Neophytos Neophytou, Xanthippi Zianni, Hans Kosina, Stefano Frabboni, Bruno Lorenzi, and Dario Narducci. Simultaneous increase in electrical conductivity and seebeck coefficient in highly boron-doped nanocrystalline si. *Nanotechnology*, 24(20):205402, 2013.
- [53] Joachim Paier, Martijn Marsman, and Georg Kresse. Dielectric properties and excitons for extended systems from hybrid functionals. *Phys. Rev. B*, 78:121201, Sep 2008.
- [54] Yanzhong Pei, Zachary M. Gibbs, Andrei Gloskovskii, Benjamin Balke, Wolfgang G. Zeier, and G. Jeffrey Snyder. Optimum carrier concentration in n-type pbte thermoelectrics. *Advanced Energy Materials*, 4(13):1400486–n/a, 2014. 1400486.
- [55] Yanzhong Pei, Aaron LaLonde, Shiho Iwanaga, and G. Jeffrey Snyder. High thermoelectric figure of merit in heavy hole dominated pbte. *Energy Environ. Sci.*, 4:2085–2089, 2011.
- [56] Yanzhong Pei, Aaron D. LaLonde, Heng Wang, and G. Jeffrey Snyder. Low effective mass leading to high thermoelectric performance. *Energy Environ. Sci.*, 5:7963–7969, 2012.
- [57] S. Poncé, E.R. Margine, C. Verdi, and F. Giustino. Epw: Electron-phonon coupling, transport and superconducting properties using maximally localized wannier functions. *Computer Physics Communications*, 209:116 – 133, 2016.
- [58] Bo Qiu, Zhiting Tian, Ajit Vallabhaneni, Bolin Liao, Jonathan M Mendoza, Oscar D Restrepo, Xiulin Ruan, and Gang Chen. First-principles simulation of electron mean-free-path spectra and thermoelectric properties in silicon. *EPL (Europhysics Letters)*, 109(5):57006, 2015.
- [59] IUrii Isaakovich Ravich. *Semiconducting lead chalcogenides*, volume 5. Springer Science & Business Media, 2013.
- [60] Yu. I. Ravich. Band Structure and Scattering Mechanisms in Lead Chalcogenides From Transport Phenomena. *Le J. Phys. Colloq.*, 29(C4):C4–114–C4–124, 1968.
- [61] Yu. I. Ravich, B. A. Efimova, and V. I. Tamarchenko. Scattering of Current Carriers and Transport Phenomena in Lead Chalcogenides II. Experiment. *Phys. Status Solidi*, 43(2):453–469, feb 1971.

- [62] D.L. Rode. *Chapter 1 Low-Field Electron Transport*, volume 10 of *Semiconductors and Semimetals*. Elsevier, 1975.
- [63] M Schlüter, G Martinez, and Marvin L Cohen. Pressure and temperature dependence of electronic energy levels in pbse and pbte. *Physical Review B*, 12(2):650, 1975.
- [64] David J. Singh. Doping-dependent thermopower of pbte from boltzmann transport calculations. *Phys. Rev. B*, 81:195217, May 2010.
- [65] Jonathan M Skelton, Stephen C Parker, Atsushi Togo, Isao Tanaka, and Aron Walsh. Thermal physics of the lead chalcogenides pbs, pbse, and pbte from first principles. *Physical Review B*, 89(20):205203, 2014.
- [66] Qichen Song, Jiawei Zhou, Laureen Meroueh, David Broido, Zhifeng Ren, and Gang Chen. The effect of shallow vs. deep level doping on the performance of thermoelectric materials. *Applied Physics Letters*, 109(26):263902, 2016.
- [67] TS Stavitskaya and VA Long. Ba efimova fizika tverd. tela, 7 (1965). *English transl. Soviet Phys. solid St*, 7:2062, 1966.
- [68] A. Svane, N. E. Christensen, M. Cardona, A. N. Chantis, M. van Schilfgaarde, and T. Kotani. Quasiparticle self-consistent GW calculations for PbS, PbSe, and PbTe: Band structure and pressure coefficients. *Phys. Rev. B*, 81(24):245120, jun 2010.
- [69] Gangjian Tan, Fengyuan Shi, Shiqiang Hao, Li-Dong Zhao, Hang Chi, Xiaomi Zhang, Ctirad Uher, Chris Wolverton, Vinayak P Dravid, and Mercouri G Kanatzidis. Non-equilibrium processing leads to record high thermoelectric figure of merit in pbte-srte. *Nature communications*, 7, 2016.
- [70] Zhiting Tian, Jivtesh Garg, Keivan Esfarjani, Takuma Shiga, Junichiro Shiomi, and Gang Chen. Phonon conduction in pbse, pbte, and pbte_{1-x}se_x from first-principles calculations. *Phys. Rev. B*, 85:184303, May 2012.
- [71] Zhiting Tian, Sangyeop Lee, and Gang Chen. A comprehensive review of heat transfer in thermoelectric materials and devices. *Ann. Rev. Heat Transfer*, 17:425–483, 2014.
- [72] M. van Schilfgaarde, Takao Kotani, and S. Faleev. Quasiparticle self-consistent *gw* theory. *Phys. Rev. Lett.*, 96:226402, Jun 2006.
- [73] Daryoosh Vashaee and Ali Shakouri. Improved thermoelectric power factor in metal-based superlattices. *Phys. Rev. Lett.*, 92:106103, Mar 2004.
- [74] CJ Vineis, TC Harman, SD Calawa, MP Walsh, RE Reeder, R Singh, and A Shakouri. Carrier concentration and temperature dependence of the electronic transport properties of epitaxial pbte and pbte/pbse nanodot superlattices. *Physical Review B*, 77(23):235202, 2008.

- [75] Lanqing Xu, Yongping Zheng, and Jin-Cheng Zheng. Thermoelectric transport properties of pbte under pressure. *Phys. Rev. B*, 82:195102, Nov 2010.
- [76] Oleg V Yazyev and Steven G Louie. Electronic transport in polycrystalline graphene. *Nature materials*, 9(10):806–809, 2010.
- [77] Qian Zhang, Eyob Kebede Chere, Yumei Wang, Hee Seok Kim, Ran He, Feng Cao, Keshab Dahal, David Broido, Gang Chen, and Zhifeng Ren. High thermoelectric performance of n-type pbte1-ysy due to deep lying states induced by indium doping and spinodal decomposition. *Nano Energy*, 22:572 – 582, 2016.
- [78] Qinyong Zhang, Hengzhi Wang, Qian Zhang, Weishu Liu, Bo Yu, Hui Wang, Dezhi Wang, George Ni, Gang Chen, and Zhifeng Ren. Effect of silicon and sodium on thermoelectric properties of thallium-doped lead telluride-based materials. *Nano Letters*, 12(5):2324–2330, 2012. PMID: 22493974.
- [79] W. Zwerger, L. Bönig, and K. Schönhammer. Exact scattering theory for the landauer residual-resistivity dipole. *Phys. Rev. B*, 43:6434–6439, Mar 1991.